SUPPLEMENTARY MATERIALS

Programming the Energy Landscape of 3D printed Kresling Origami via Crease Geometry and Viscosity

Samantha Mora[a], Nicola M. Pugno[a,b], Diego Misseroni[c,*]

[a] *Laboratory for Bioinspired, Bionic, Nano, Meta Materials and Mechanics, Department of Civil, Environmental and Mechanical Engineering, University of Trento, Italy*

[b] *School of Engineering and Materials Science, Queen Mary University of London, Mile End Road, London E1 4NS, UK*

[c] *Laboratory for the Design of Reconfigurable Metamaterials and Structures, Department of Civil, Environmental and Mechanical Engineering, University of Trento, Italy*

[*] *Corresponding Author (diego.misseroni@unitn.it)*

Contents

S.1 Materials and Methods

S.1.1 Initial sizing of Kresling cells

We determined an initial geometrical configuration of the Kresling cell that could potentially exhibit bistability. The approach relied on a five-parameters model incorporating the elastic deformation of stretchable mountain and valley creases [1, 2] with their rotational behavior [3]. As illustrated in Fig. S.1A, we first considered the following initial geometrical parameters: an initial height denoted by h_o, upper and lower polygons with n sides circumscribed within a radius r, an initial relative angle θ_o between these polygons. The original lengths of the creases, denoted by a_o (side of the polygon), b_o (peaks), and c_o (valleys), and their corresponding dihedral angles δ_{ao}, δ_{bo}, and δ_{co}, can be calculated using the expressions:

$$a_o = 2r \sin\left(\frac{\pi}{n}\right) \tag{1}$$

$$b_o = \sqrt{4r^2 \sin^2\left(\frac{\theta_o}{2}\right) + h_o^2} \tag{2}$$

$$c_o = \sqrt{4r^2 \sin^2\left(\frac{\theta_o + \frac{2\pi}{n}}{2}\right) + h_o^2} \tag{3}$$

$$\delta_{ao} = atan\frac{h_o}{2r \sin\left(\frac{\theta_o}{2}\right) sin\left(\frac{\theta_o}{2} + \frac{\pi}{n}\right)} \tag{4}$$

$$\delta_{bo} = \pi - acos\frac{h_o^2 cos\left(\theta_o + \frac{2\pi}{n}\right) - r^2\left[cos\left(\theta_o + \frac{\pi}{n}\right) - cos\left(\frac{\pi}{n}\right)\right]^2}{h_o^2 + r^2\left[cos\left(\theta_o + \frac{\pi}{n}\right) - cos\left(\frac{\pi}{n}\right)\right]^2} \tag{5}$$

$$\delta_{co} = \pi - acos\frac{h_o^2 cos\left(\theta_o\right) - r^2\left[cos\left(\theta_o + \frac{\pi}{n}\right) - cos\left(\frac{\pi}{n}\right)\right]^2}{h_o^2 + r^2\left[cos\left(\theta_o + \frac{\pi}{n}\right) - cos\left(\frac{\pi}{n}\right)\right]^2} \tag{6}$$

When the compressive load F is applied to the top of the Kresling cell, it produces an axial displacement u and a twisting rotation ϕ between the upper and lower polygons, while the final height of the Kresling cell becomes h, as shown in Fig. S.1A. Furthermore, the length of the crease corresponding to the side length of the polygon a_o remains constant with negligible deformation, as it remains circumscribed within the polygon's circle of radius r. At this stage,

it can be considered that $a = a_o$, and the lengths of the creases corresponding to the peaks, b, and valleys, c with their respective dihedral angles δ_a, δ_b, and δ_c are defined as follows:

$$b = \sqrt{4r^2 \sin^2\left(\frac{\phi}{2}\right) + (h_o - u)^2} \tag{7}$$

$$c = \sqrt{4r^2 \sin^2\left(\frac{\phi + \frac{2\pi}{n}}{2}\right) + (h_o - u)^2} \tag{8}$$

$$\delta_a = atan\frac{h_o - u}{2rsin\left(\frac{\phi}{2}\right)sin\left(\frac{\phi}{2} + \frac{\pi}{n}\right)} \tag{9}$$

$$\delta_b = \pi - acos\frac{(h_o - u)^2 cos\left(\phi + \frac{2\pi}{n}\right) - r^2\left[cos\left(\phi + \frac{\pi}{n}\right) - cos\left(\frac{\pi}{n}\right)\right]^2}{(h_o - u)^2 + r^2\left[cos\left(\phi + \frac{\pi}{n}\right) - cos\left(\frac{\pi}{n}\right)\right]^2} \tag{10}$$

$$\delta_c = \pi - acos\frac{(h_o - u)^2 cos\,(\phi) - r^2\left[cos\left(\phi + \frac{\pi}{n}\right) - cos\left(\frac{\pi}{n}\right)\right]^2}{(h_o - u)^2 + r^2\left[cos\left(\phi + \frac{\pi}{n}\right) - cos\left(\frac{\pi}{n}\right)\right]^2} \tag{11}$$

During the compression process, the total elastic energy stored in the creases, denoted as U, can be calculated as the sum of the deformation energy of the peaks and valleys, U_b, and the contribution from the rotational springs of the creases, U_s, as given by the following expressions, which are defined by five parameters: b, c, δ_a, δ_b and δ_c.

$$U_b = \frac{1}{2}nK_{sb}(b - b_o)^2 + \frac{1}{2}nK_{sc}(c - c_o)^2 \tag{12}$$

$$U_s = \frac{1}{2}nK_a(\delta_a - \delta_{ao})^2 + \frac{1}{2}nK_b(\delta_b - \delta_{bo})^2 + \frac{1}{2}nK_c(\delta_c - \delta_{co})^2 \tag{13}$$

$$U = U_b + U_s \tag{14}$$

Here, K_{sb} and K_{sc} represent the stretching stiffness of the peaks and valleys, respectively, while the rotational stiffness of the creases is represented by K_a for the side polygon, K_b for the peaks, and K_c for the valleys. The total potential energy in the Kresling cell, $\Pi(u)$, can be determined by the sum of the total elastic energy stored in the creases U, and the work done by

the external force F that produces an axial displacement u:

$$\Pi(u) = U - Fu \tag{15}$$

If we adhere to the principle of minimum total potential energy, we can identify an equilibrium state [4]. Thus, we assume that:

$$\delta\Pi/\delta u = 0 \tag{16}$$

Then, we can define the applied axial force F, under the mentioned equilibrium conditions and in terms of the total elastic energy stored energy in the creases, as follows:

$$F = \delta U/\delta u \tag{17}$$

The previously mentioned equations enabled a preliminary evaluation of various geometrical configurations to determine the initial sizing of a Kresling cell. The energy landscapes calculated from Eq. 14, determined which initial geometrical parameters can be used to shape Kresling cells prone to ensure a second local of energy minimum and satisfying the condition $\delta U/\delta u = 0$, for further analyses. The geometrical configurations considered in this preliminary assessment include: aspect ratios h_o/r within the range of 0.4 to 2.25, polygons with a number of sides equal to n=6 and initial rotational angles θ_o ranging from $\pi/4n$ to $3\pi/n$ ($7.5° \leq \theta_o \leq 90°$). The total elastic energy stored in the creases U, and axial displacement u, were normalized to represent dimensionless quantities in the plots.

The stretching stiffness K_s is defined in terms of Young's modulus E, and cross-sectional area A as $K_s = EA$. By defining the stretching stiffness of the peaks and valleys per unit length, we obtain $K_{sb} = K_s/b_o$ and $K_{sc} = K_s/c_o$, respectively. Similarly, the rotational stiffness K, can be also expressed per unit length, with $K_b = Kb_o$ for the peaks and $K_c = Kc_o$ for the valleys. For this initial analysis, the contributions of both stiffness components to the total elastic energy were introduced as three different ratios: $K/K_s = 0, 0.5x10^{-4}, 1.0x10^{-4}$. As a result, two main scenarios were observed during the compression process of the Kresling cells: Bistability (Bi) and Monostability (M), as illustrated in the plots of Fig. S.1B. When considering a rotational stiffness $K = 0$, the results correspond to those obtained by the bar and truss model defined by two parameters, (b,c).

Configurations with an initial rotational angle within the range $15° \leq \theta_o \leq 60°$ and an aspect ratio $h_o/r \geq 1.5$ exhibited an apparent bistability. Those Kresling cells showed

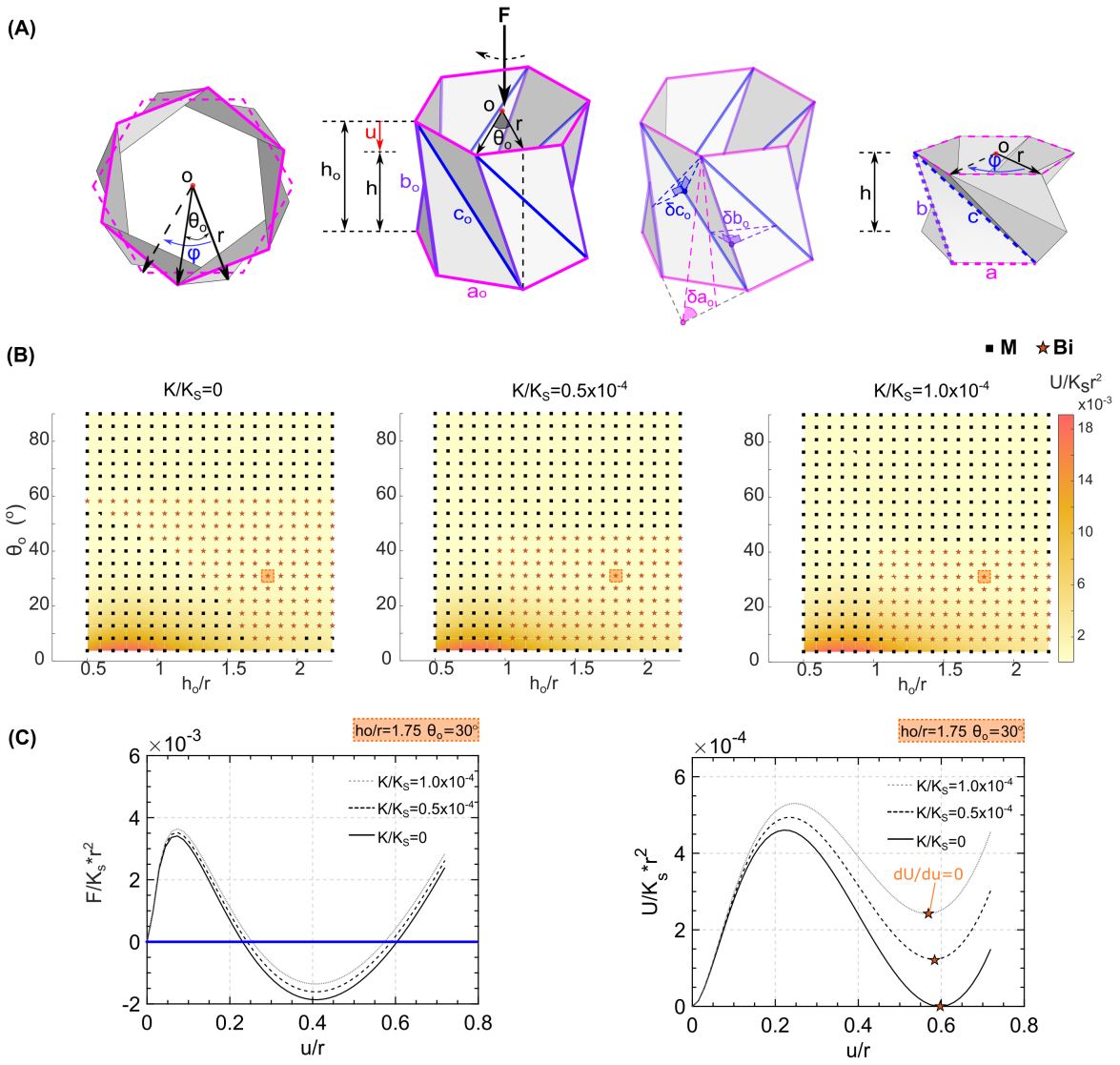

Figure S.1: Initial sizing of the Kresling cell. **(A)** Kresling cell geometrical parameters during compression/expansion process. **(B)** Initial assessment of monostable (M) and Bistable (Bi) configurations through a five-parameters model, by considering their initial relative angle θ_o and aspect ratio h_o/r and rotational versus stretching stiffness ratio K/K_s. (C) Normalized Force (F) and Energy (U) plots versus normalized displacement u/r of the configuration $\theta_o = 30^o$ and h_o/r=1.75.

normalized energy landscapes with a second local of energy minimum ($\delta U/\delta u = 0$). In addition, we observed that the majority of configurations with initial rotational angles lower than $\theta_o = 40°$ and h_o/r <1.5 tended to present a monostable behavior. While those with higher values, $\theta_o > 60°$, allowed small rotational displacements limiting the folding process and the panels tended to overlap prematurely. In contrast, Kresling cells with initial relative angles $\theta_o < 7.5°$, were prone to buckle during the initial folding stages, displaying an almost rigid behavior and higher energy values. Furthermore, Fig. S.1C presents the corresponding normalized force and elastic energy landscapes obtained for the configuration: $\theta_o = \pi/6$, and h_o/r=1.75. It exhibited a potential tendency towards bistability in all the evaluated scenarios

$(K/K_s = 0, 0.5x10^{-4}, 1.0x10^{-4})$. Thus, we selected these geometrical parameters for the initial sizing of the Kresling cells used in the subsequent analyses.

S.1.2 Parametric design of 3D Kresling cells

The 3D CAD parametric models were generated in Autodesk Inventor following the initial geometrical configuration: polygons with n = 6 sides, initial relative angle $\theta_o = \pi/6$, initial height versus radius ratio h_o/r=1.75, and panels thickness $\overline{s} \approx 0.04h_o$. The parametric design process is summarized in Fig. S.2. Firstly, the upper and lower polygons are defined in 2D sketches and rotating with respect to each other in an angle equal to $\theta_o = 30°$. The panels thickness $\overline{s}$ was defined through an offset to the polygons' perimeter and the width limit of the creases was determined by auxiliary circles with radius r'. Then, 3D sketches were constructed to enable the 3D structure of the panels, and by using the command Boundary-surface their profiles can be linked to form the surfaces of the panels. Next, the surfaces were merged with the Patch command, and volumetric bodies were obtained to shape the panels and the creases. As a result we obtained a 3D Kresling cell which represent the intact crease case.

The creases were designed with gradual reductions in their cross-sections, preserving a V shape at the top and a variable circular shape at the bottom. A cutting radius $s_c = r'.RF$ is defined according to the imposed reduction factors from $0.25 \leq RF \leq 0.80$, decreasing the external thickness s and an internal thickness s_i is obtained. Afterwards, the 3D CAD model were saved as *.step files for the Abaqus/CAE numerical simulations.

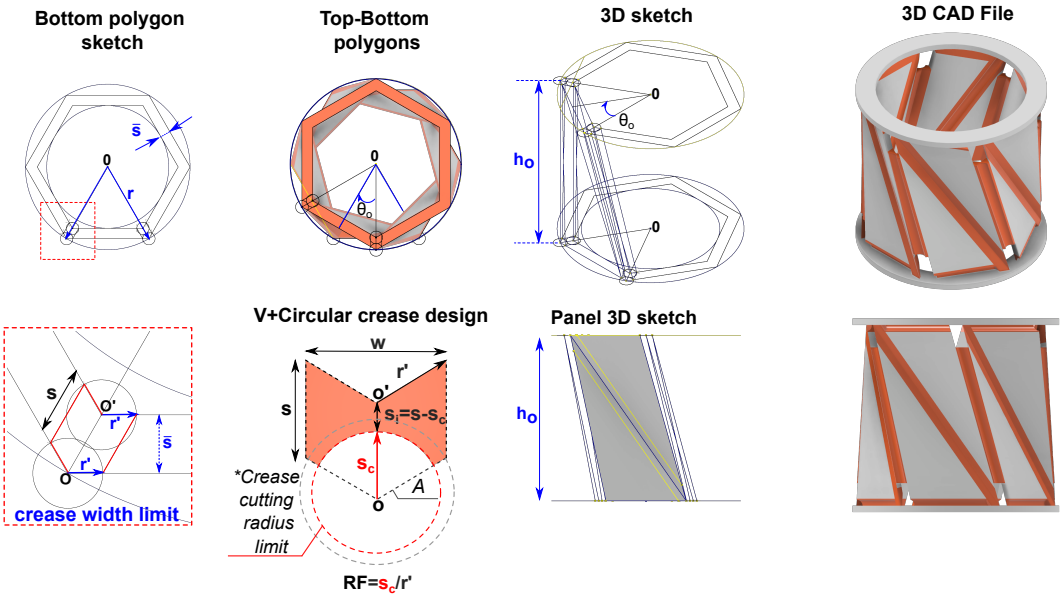

Figure S.2: Parametric design process of a 3D Kresling cell. Creation of former 2D and 3D sketches in Autodesk Inventor.

S.1.3 Numerical simulations considerations

The entire modeling process for simulating the kinematics of Kresling cells and generating the load paths for the parametric study is schematized in Fig. S.3. The input 3D CAD files for the Kresling cells models were saved as *.step files to be imported from Abaqus/CAE Standard for their assembly. Traditionally, 3D printed Kresling cells have been designed and modeled as linear elastic shells. This is particularly applicable to polymeric sheets with thicknesses less than 1 mm, while also considering the use of rigid or flexible materials. However, employing rubbery creases, which are treated as nearly incompressible material, requires the use of hyperelastic models with 3D hybrid modified formulation elements to achieve more realistic results.

In addition, complex and irregular 3D geometries such as Kresling inspired structures, require the use of tetrahedron elements besides the application of free mesh with partition strategies. Thus, intricate shapes can be accurately modeled while maintaining computational efficiency at the same time. Given the hyperelastic nature of the flexible Polyjet photopolymers, the selected mesh was composed by 10 node quadratic tetrahedron with hybrid modified constant pressure elements C3D10MH. An adaptive mesh refinement study determined a suitable mesh density that enables the achievement of convergence within a balanced computational time.

Four types of tetra-mesh from a coarse to refined number of elements were analyzed comparing their obtained maximum force, that leads to the highest stress concentrations on the Kresling cell, as well as the CPU time and refinement error ($R_E(\%)$), as described in Fig. S.4. The latter was obtained by using the expression: $100\,(F_{Mi} - F_{M4})/F_{M4}$, where F_{Mi} represents the maximum force obtained in the numerical simulation with each mesh case i, F_{M4} is the maximum force from the last attempt corresponding to the very refined mesh case M4. The selected mesh corresponded to the case M3, which is formed by minimum three elements assigned across the panels and creases cross-sections. This refined mesh fitted more accurately to the Kresling cell geometry, reducing modeling errors and ensuring convergence.

Moreover, kinematic couplings were assigned between the reference points RP and the top and bottom ring surfaces to effectively transmit the applied displacement, and the assigned boundary conditions along the entire cylinder. The constitutive models used in the analyses included an elasto-plastic model for the rigid photopolymers assigned to the panels, and a visco-hyperelastic model for the flexible materials assigned to the creases.The material characterization data necessary to define these constitutive models were obtained through uniaxial tests, detailed in the following sections S.1.5 and S.1.6, and summarized in Tables 1

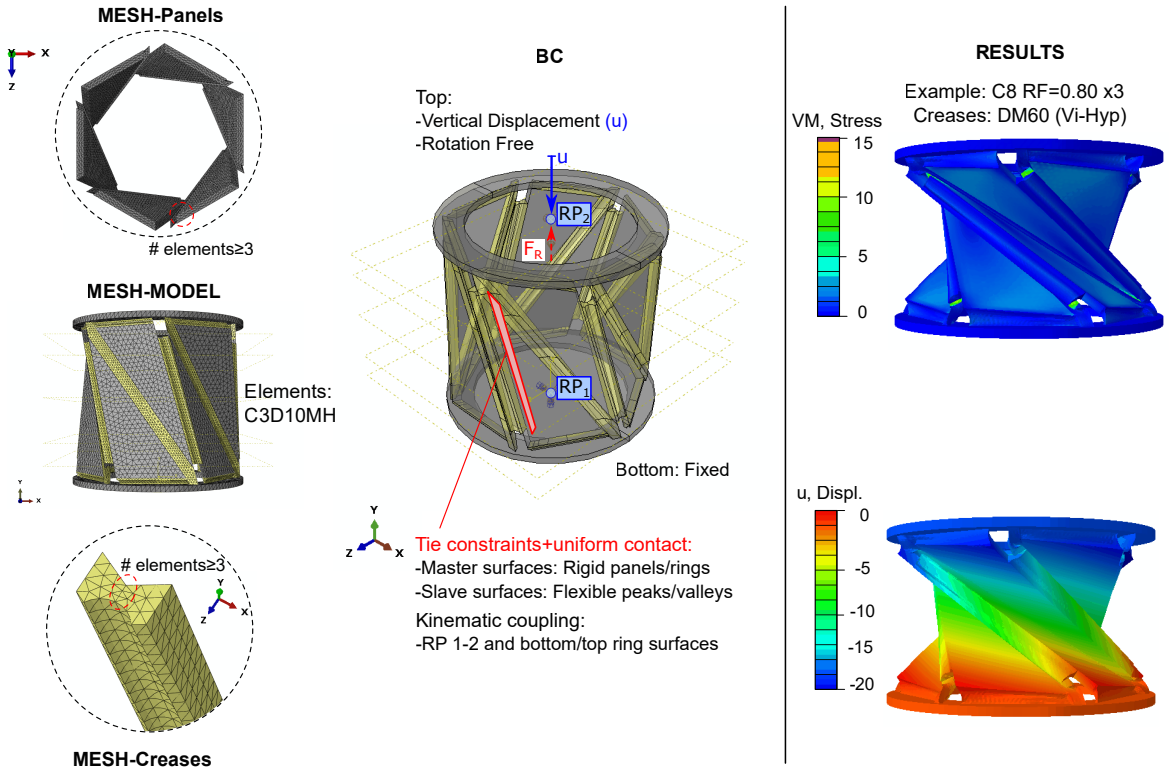

Figure S.3: Numerical simulations process in Abaqus/ CAE Standard. Mesh generation, boundary conditions (BC) and example of obtained results in terms of Von Mises stress in MPa, VM, and vertical displacement, u, in mm. $*RP_2$ represents the reference point where the vertical displacement is applied, generating a restoring force F_R considered for the load path plots.

and 2.

Furthermore, tie constraints were used to create a uniform contact among the panels, creases, top and bottom ring surfaces. Fixed boundary conditions were applied at the bottom of the cylinder, specifically at reference point RP_1, to restrict displacements and rotations in all directions. A vertical displacement, u, approximately equal to one third of the initial height of the Kresling cells ($\approx 1/3\, h_o$), was imposed at the top in the respective reference point RP_2 and the corresponding applied Force was computed to determine the respective force/displacement curves. This target displacement prevents further overlapping of the panels during the compression of the Kresling cell.

The rotation at the top was released to simulate the natural twisting plus compression motion of Kresling cells. A VISCO step was used to perform quasi-static analyses, incorporating time-dependent material behavior without inertia effects. The geometric nonlinearity option (NLGEOM) was activated to consider large deformations in the analysis. We first focus on the initial relaxation region of the analyzed rubbery materials within a time defined as τ_i^*, during which most of the stress decay occurs, as shown in Fig.4B, to observe the viscosity effects during bistability achievement. Then, the total simulation duration t_t was estimated to lie within

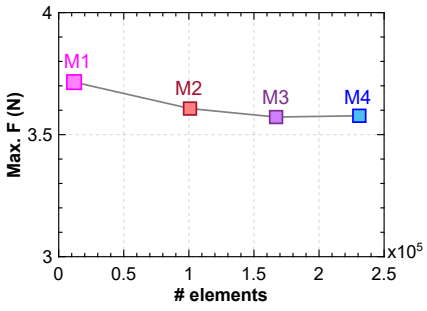

Mesh	# elements	Cr_s	PA_s	CPU_{time} (s)	R_E (%)
M1	11816	1.10	1.00	731	3.85
M2	100877	0.30	0.60	23104	0.83
M3	167011	0.25	0.50	25318	-0.15
M4	230964	0.20	0.40	60982	-

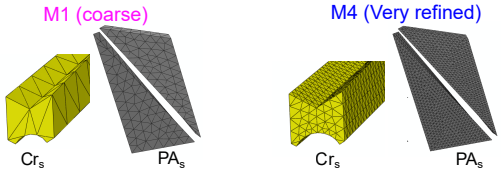

Figure S.4: Mesh refinement study parameters. Based on the maximum force achieved, Max(F), total number of elements, including number of seeds along creases (cr_s) and panels (PA_s), CPU time in seconds and refinement error percentage ($R_E(\%)$).

this initial relaxation region by using a velocity of 0.1 mm/s to reach the target displacement u. The VISCO step was defined with a initial time size set to $0.01t_t$, while the maximum and minimum increments were $0.1t_t$ and 10^{-6}, respectively. Thus, we can accurately capture the viscosity effects and ensure the convergence by reducing the number of increments in the solver. In addition, we performed simulations for each rubbery material over extended time periods to predict whether bistability can also be achieved in both short- and long-term relaxation regions. For instance, to determine the total simulation duration t_t for the short-term relaxation region, we considered a reference time τ equal to the highest τ_i term from the Prony series described in Table 2. In this region, a lower stress decay in the relaxation curve of each rubbery material was also observed. For long-term effects, when the material is fully relaxed and the stress relaxation curve approaches a horizontal asymptote, we used total simulation durations t_t of nτ, with n=6.

S.1.4 Design and Fabrication of samples for tensile tests

Polyjet photopolymers main groups can be classified into rigid thermoplastics, rubbers and a hybrid types of composites, so called Digital Materials. The latter represent a combination between glassy and flexible polymers, with various levels of shore hardness from A30 to A95. In the present study, the selected rigid photopolymers were VeroYellow, VeroBlack and Digital ABS. The tested rubbery Digital Materials were: AgilusClear 30 (Shore A30), FLXA-YT-S60 DM (Agilus30 + Vero Yellow, Shore A60), FLXA-9970 DM (Agilus30 + VeroClear, Shore A70), FLXA-9985 DM (Agilus30 + VeroClear, Shore A85) and FLXA-YT-S95 DM (Agilus30 + VeroYellow, Shore A95). In this study they are referred with the acronyms AG30, DM60, DM70, DM85 and DM95, respectively.

All the samples were fabricated using a 3D printer Stratasys J750 with a layer resolution of approximately 27 microns in High-Mix mode. The support material was first smoothed in a soapy water solution bath for one hour and then, it was removed using water jetting.

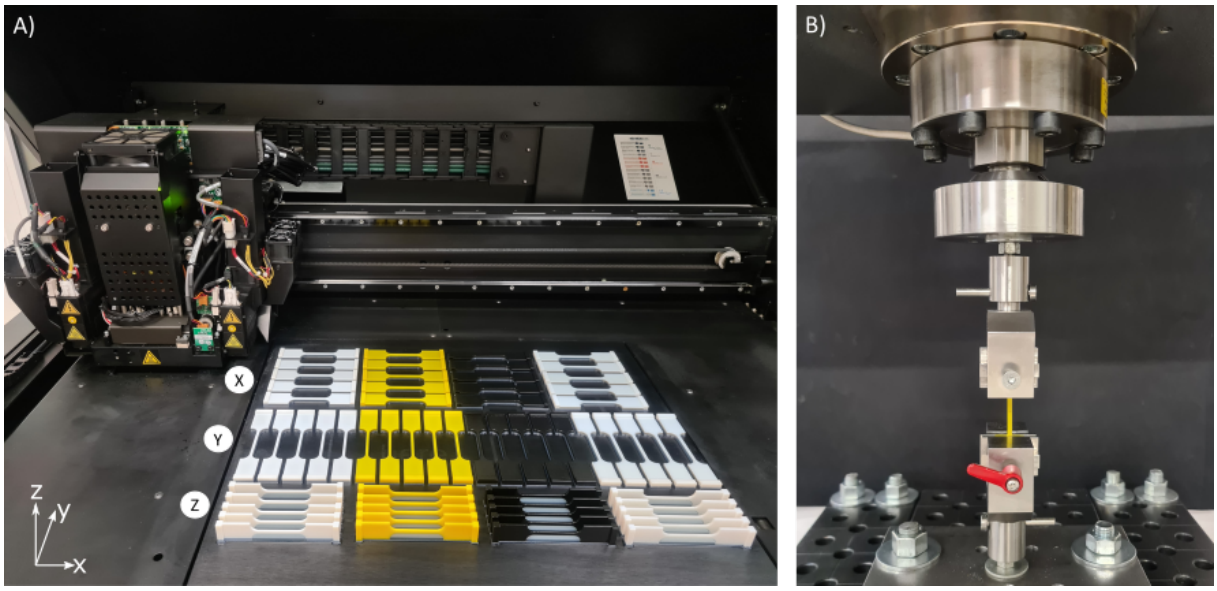

Figure S.5: Specimens made of photopolymers for uniaxial tests. **(A)** Fabrication via Polyjet technique with orientations along the X,Y,Z axis of the build tray. **(B)** Experimental setup for uniaxial tests.

For the uniaxial tensile tests, dog-bone-shaped samples were designed following the ASTM D638 standard for rigid polymers, and the ASTM D412 standard for rubbers. Five samples were fabricated for each material type. They were printed in three directions: longitudinal (X), transversal (Y) and perpendicular (Z) to the build tray, as shown in Fig. S.5A. For the stress relaxation tensile tests conducted on the rubbery material, dog-bone sample design adhered to the ISO 6914, ASTM E328, and ASTM D412 standards. Three samples were printed longitudinally oriented to the build tray for each type of Digital Material.

S.1.5 Uniaxial tensile tests and constitutive models

The uniaxial tests were carried with a MIDI 10 testing machine by imposing a cross-head velocity of 0.1 mm/sec, as shown in Fig. S.5B. The tests stopped when fracture occurred in the sample. During the test both applied displacement and load were recorded. In particular, two types of load cells with different capacities were used to measure the applied tensile load during the experiments: 100kN for rigid polymers, and 10 kN for rubbery materials. The data rate acquisition was equal to 1 sample/sec. The constitutive models employed in the numerical simulations, were obtained based on experimental data from the previously mentioned uniaxial tests. The average among the different printing orientations, in X,Y and Z, was considered for the mechanical properties estimation. In the case of rigid photopolymers, such as VeroBlack (VB), an elasto-plastic model was selected. The average stress-strain curves and Young's modulus are shown in Fig. S.6A and B, respectively. The Young's Modulus was estimated

from the slope of the $\sigma - \varepsilon$ curves within the elastic range. The latter is determined by fitting a straight trendline to the experimental curve, which extends from the beginning of the curve to the point where the R^2 values approach closest to 1. The elasto-plastic behavior was modeled in Abaqus/CAE standard, considering the experimental $(\sigma - \varepsilon)$ curves by using the material calibration utility.

First, the nominal $(\sigma - \varepsilon)$ curves inputs get converted into true strains (ε_t) and true stresses (σ_t) with the expressions: $\varepsilon_t = ln(1 + \varepsilon)$ and $\sigma_t = \sigma(1 + \varepsilon)$. The Young's modulus is calculated as previously explained and used as an input datum. Thus, the yield point can be identified and the plastic strains, ε^{PL}, and stresses, σ^{PL}, are finally estimated to characterize the elasto-plastic model: $(\varepsilon = \varepsilon^{EL} + \varepsilon^{PL})$. Moreover, we evaluated the loss of mechanical properties over time of rigid photopolymers from the Vero group, such as VeroBlack (VB). Similarly, samples were fabricated and tested one day, one and six months after, following the mentioned uniaxial test procedure.

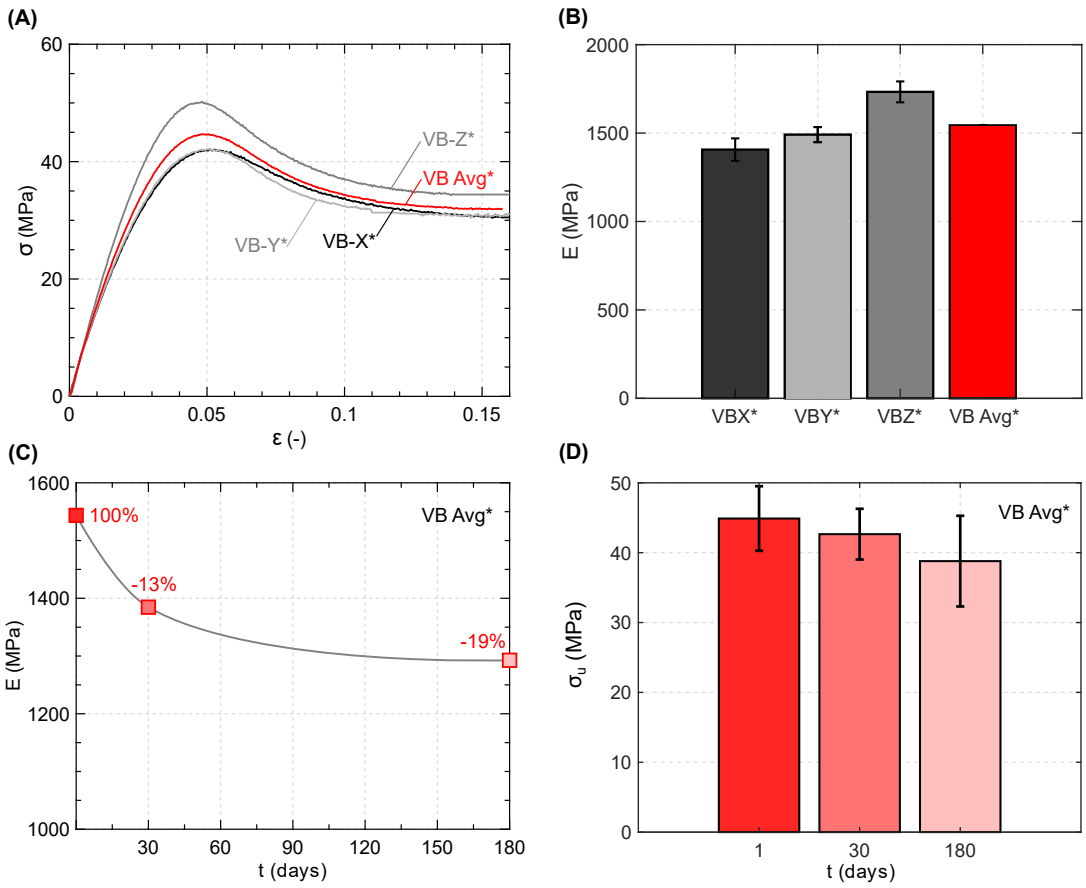

Figure S.6: VeroBlack experimental data. **(A)** Average Stress-Strain $(\sigma - \varepsilon)$ plots. **(B)** Average Young's modulus E +/- standard deviation obtained per each group of samples with a printing orientation in X, Y, and Z axis, and overall average (VB Avg*). Loss of mechanical properties, including: **(C)** Young's modulus, E, and **(D)** Ultimate tensile strength, σ_u, due to aging effects analyzed using data obtained from tests conducted after 1 (E=100%), 30, and 180 days of sample fabrication.

Rubbery materials are mostly defined by strain energy potential functions due to their hyperelastic behavior. Their mechanical characterization requires a further step to find a model that fits the nominal curves ($\sigma - \varepsilon$) with the tensile tests of the Digital materials group: AG30, DM60, DM70, DM85 and DM95. Considering that the experimental data was obtained from uniaxial tests, the material constants C_{ij} from linear hyperelastic polynomial models were fitted to the nominal stresses. Thus, they were calculated through a least-squares method in Abaqus/CAE material model calibration tool [5]. Then, the relative error (RE) of the stress measure is minimized and it is defined by the expression:

$$RE = \sum_{i=1}^{n} \left(1 - \frac{\sigma_i^{th}}{\sigma_i^{exp}}\right)^2, \tag{18}$$

where σ_i^{exp} represents the experimental stress measures and σ_i^{th} is the nominal stress. In this case, the latter is determined by the tensile uniaxial stress T_1, which is derived from the strain energy potential U and the stretch in the loading direction λ_1, as follows:

$$T_1 = 2(1 - \lambda_1^{-3})\left(\lambda_1 \frac{\partial U}{\partial \overline{I_1}} + \frac{\partial U}{\partial \overline{I_2}}\right) \tag{19}$$

Thereby, a Neo-Hookean model fitted the nominal stresses of the tested digital materials group from AG30, DM60 to DM95 as Fig. S.7A depicts. The fitting was obtained with relative errors between the range $5\% \leq RE \leq 10\%$. Moreover, this strain energy function is described in Invariant base form as: $U_N = C_{10}(\overline{I_1} - 3)$, and its equivalent stretch base is written as:

$$U_N = \frac{\mu_{10}}{2}(\lambda_1^2 + \lambda_2^2 + \lambda_1^{-2}.\lambda_2^{-2} - 3), \tag{20}$$

Additional mechanical properties, including average elongation at break (ε_b), were determined from the experimental curves ($\sigma - \varepsilon$), as shown in Fig. S.7B. Other hyperelastic models, such as Mooney-Rivlin and Polynomial N=1, showed higher relative error values ranging from $10\% \leq RE \leq 32\%$, and they also presented unstable strains during the calibration process.

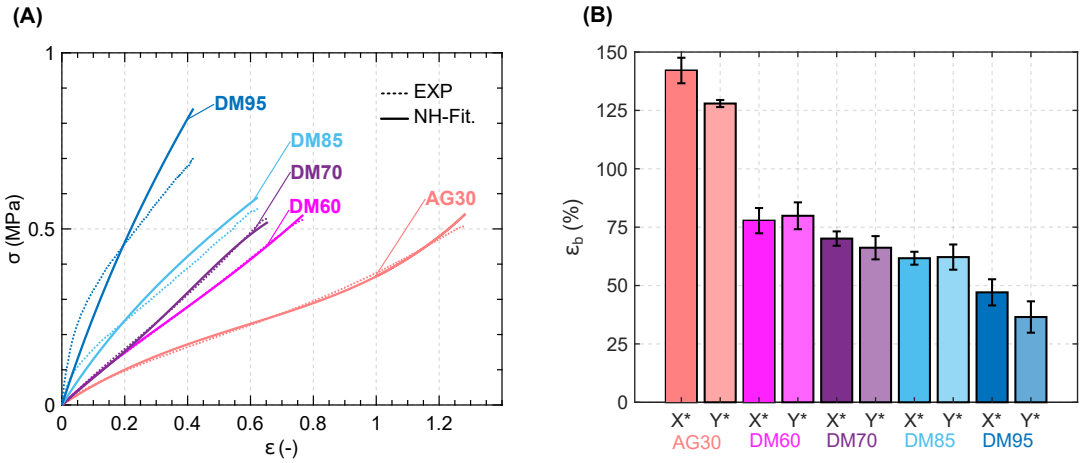

Figure S.7: Rubbery Digital materials (DM) experimental data. **(A)** Average stress-strain curves obtained during the uniaxial tests (Exp) and hyperelastic models fitting with Neo-Hookean (NH-Fit) strain energy potential. **(B)** Average Elongation at break, ε_b, +/- standard deviation. (*) Average obtained per each group of samples with a printing orientation in X and Y axis.

S.1.6 Stress Relaxation tests and Viscoelastic parameters

Rubbery materials present high sensitivity to strain rates and time-dependent behavior, which can be further characterized by a visco-hyperelastic model. The time dependent constitutive equations that define linear viscoelastic materials, are based on the stress and strain history, loading-displacement rate and loading application time. Polyjet elastomers usually exhibit a significant relaxation of their peak stresses in a short time span, some of them reaching it in 20 seconds [6].

The most common viscoelastic models are based on the combination in series or in parallel of linear elastic (springs) and viscous components (dashpots). Then, the viscoelastic components can be determined by conducting a stress relaxation test and therefrom, obtaining the subsequent Prony parameters. The load and time data considered for determining the viscoelastic properties are recorded once the imposed strain value ε_0 is reached. The initial part of loading phase, where the strain is rapidly increasing, is usually disregarded. After this initial phase, a time t=0 is established as the starting point for analysis under a constant strain ε_0, together with an initial stress σ_0 and the corresponding elastic instantaneous modulus E_o. Therefore, the time dependent stress $\sigma(t)$ is defined by:

$$\sigma(t) = E(t)\varepsilon_o \tag{21}$$

Considering that the material behaves as a Maxwell solid, the time dependent relaxation modulus E_t can be expressed in terms of a Prony series expansion and calculated from E_o [7],

as shown below:

$$E(t) = E_o\left(1 - \sum_{i=1}^{N} E_i(1 - e^{-t/\tau_i})\right) \tag{22}$$

where E_i corresponds to the "i-th" Prony coefficient, N represents the total number of terms of the Prony series, and τ_i is the relaxation time constant. Thereby, the Tensile relaxation modulus $E(t)$, can be determined by $E(t) = \sigma(t)/\varepsilon_0$. Then, the Shear relaxation modulus $G(t)$, can be obtained by the expression: $G(t) = E(t)/\left[2(1+\nu)\right]$ and the corresponding values per each analyzed rubbery photopolymer are illustrated in Fig. S.8A. Furthermore, the tensile instantaneous relaxation modulus E_o, corresponding to the time t=0, is defined by $E_o = \sigma_0/\varepsilon_0$. Similarly, the shear instantaneous relaxation modulus G_o, is calculated by $G_o = E_o/[2(1+\nu)]$. The Poisson's ratio ν of elastomeric photopolymers and composites with shore hardness between DM60 and DM95, can vary from 0.48 to 0.46, and 0.49 for the rubbery AG30 [8]. The rate-independent behavior of the material can be defined as hyperelastic under large strains in Abaqus/CAE solvers and being described by the instantaneous relaxation tensile modulus. After, we estimated a normalized shear relaxation modulus from the experimental curve $(G(t) - t)$ employing the expression: $G_n = G(t)/G_0$. Thus, Eq. 22 can be re-written in terms of the normalized shear relaxation modulus $G_n(t)$, and the dimensionless Prony constants g_i, as follows:

$$G_n(t) = 1 - \sum_{i=1}^{N} g_i(1 - e^{-t/\tau_i}) \tag{23}$$

In addition, the long-term shear relaxation modulus G_∞ is defined by the shear instantaneous relaxation modulus G_o and the dimensionless Prony constants g_i, as given by Eq. 22:

$$G_\infty = G_o\left(1 - \sum_{i=1}^{N} g_i\right) \tag{24}$$

Assuming a linear viscosity and nearly incompressibility of the material, given that the Poisson's ratio of the studied rubbery materials ranges within 0.46 and 0.49, the long-term tensile relaxation modulus can be estimated as: $E_\infty = G_\infty[2(1+\nu)]$.

The viscoelastic material properties, defined by the dimensionless Prony series parameters, can be determined by fitting them to experimental relaxation test data. For this reason, a series of stress relaxation tests in tension were performed by adapting the ISO 6914 and ASTM E328 standards. Three different constant strain values, $\varepsilon_0 = 10\%$, $\varepsilon_0 = 15\%$, and $\varepsilon_0 = 25\%$, were imposed on each rubbery sample.

The stress relaxation tests for rubbery materials were conducted with a MIDI 10 testing machine by imposing a cross-head velocity of 0.1 mm/sec and at controlled room temperature (23 °C). A 10 kN load cell measured the applied tensile load. When the displacement corresponding to the target strain was reached, the machine stopped and the load relaxation was monitored. At this point, an initial time $t = 0$ is established in the force-time curve (F-t), along with its corresponding peak force F_o and a constant strain ε_o. The tests were considered concluded when the force-time curve $(F - t)$ approached an almost horizontal asymptotic line.

Subsequently, the stress depending on time $\sigma(t)$ was calculated by dividing the force $F(t)$ by the cross-sectional area of the sample A_o. This conversion transformed the force-time $(F - t)$ curve into a stress-time $(\sigma - t)$ curve, which begins at the peak stress σ_o. Next, the average $(\sigma - t)$ curves for each group of samples subjected to constant strain values, $\varepsilon_0 = 10\%$, $\varepsilon_0 = 15\%$, and $\varepsilon_0 = 25\%$, were obtained. Since the Kresling creases are designed to overcome large deformations, and ISO 6914 standards recommend the use of high strain values, we selected the maximum strain value (ε_o=25%) for estimating the Relaxation modulus and the Prony series parameters. The difference between the $G(t)$ and $G_n(t)$ curves obtained from the average values and the selected maximum strain (ε_o=25%) was not significant. We then applied these obtained Prony coefficients to the constants within the strain energy function $U_N(t)$ in order to introduce the rate-dependent behavior associated with viscosity. Consequently, in the case of a Neo-Hookean material model defined by an instantaneous constant C_{10}^o, the visco-hyperelastic relaxation function can be expressed as follows:

$$U_N(t) = C_{10}^o \left(1 - \sum_{i=1}^{N} g_i (1 - e^{-t/\tau_i}) \right) \tag{25}$$

These parameters are then incorporated into a visco-hyperelastic constitutive model described by Eq. 25 for subsequent numerical simulations in Abaqus/CAE. Then, we fitted the obtained Prony parameters to the experimental data $(G_n - t)$ using a damped least squared method (DLS). It was implemented using a Matlab optimization toolbox script based on the Levenberg–Marquardt algorithm. As a result, the selected fitting coefficients correspond to the lowest goodness of fit values, as shown in Fig. S.8B. The latter is obtained from the norm of residuals, denoted as $\|e\|$ and calculated as follows:

$$\|e\| = \sqrt{\sum_{i=1}^{n} e_i^2}, \tag{26}$$

where the residuals e_i represent the sum of the differences between the observed y_i and predicted values $f(x_i)$, being defined as: $e_i = y_i - f(x_i)$.

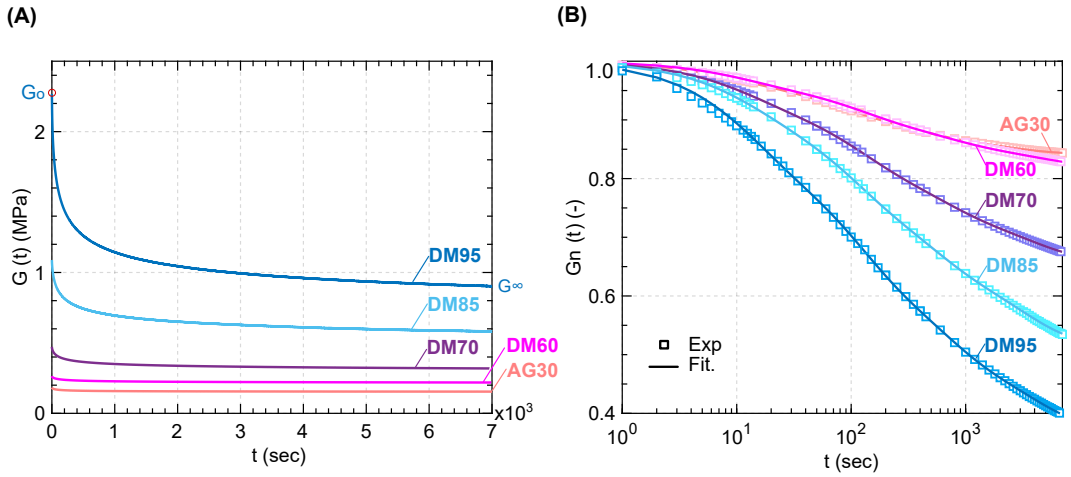

Figure S.8: Stress relaxation tests of the Rubbery Digital Materials AG30 to DM95. (A) Relaxation function G(t) with the corresponding Instantaneous modulus G_o. Units: MPa. **(B)** Experimental and fitted data of the Normalized shear relaxation modulus $G_n(t)$, in logarithmic scale with their respective goodness of fit in terms of the norm of residuals $||e||$, where: AG30 $||e|| = 3.9x10^{-4}$, DM60 $||e|| = 4.0x10^{-4}$, DM70 $||e|| = 5.8x10^{-4}$, DM85 $||e|| = 3.1x10^{-3}$, DM95 $||e|| = 2.5x10^{-3}$.

Material	**E (MPa)**	σ_y **(MPa)**	ε_b **(%)**	σ_u **(MPa)**
VeroBlack	1543.58	19.79	15.75	44.89
UTL Resin (BMF)	567.00	10.00	40.80	14.10
Origin 402	42.00	-	230	5.5
IP-PDMS	15.30	-	240	-

Table 1: Elastic and Elasto-plastic materials mechanical properties.

AG30		**DM60**		**DM70**		**DM85**		**DM95**	
$C_{10} = 0.111$		$C_{10} = 0.157$		$C_{10} = 0.163$		$C_{10} = 0.237$		$C_{10} = 0.457$	
$E_o = 0.545$		$E_o = 0.782$		$E_o = 1.398$		$E_o = 3.200$		$E_o = 6.621$	
$E_\infty = 0.459$		$E_\infty = 0.651$		$E_\infty = 0.938$		$E_\infty = 1.676$		$E_\infty = 2.498$	
$G_o = 0.183$		$G_o = 0.268$		$G_o = 0.479$		$G_o = 1.095$		$Go = 2.267$	
$G_\infty = 0.154$		$G_\infty = 0.220$		$G_\infty = 0.317$		$G_\infty = 0.570$		$G_\infty = 0.855$	
g_i	τ_i	g_i	τ_i	g_i	τ_i	g_i	τ_i	g_i	τ_i
0.030	7.612	0.035	10.350	0.060	10.717	0.071	10.787	0.143	11.435
0.052	64.359	0.055	98.390	0.099	93.980	0.132	78.847	0.189	93.977
0.045	333.610	0.048	547.863	0.090	498.890	0.131	404.112	0.154	520.646
0.030	2310.2422	0.041	4151.017	0.089	3632.445	0.146	3116.457	0.137	3697.450

Table 2: Flexible materials mechanical properties and Prony series parameters. *E_o, E_∞, G_o, G_∞ units in MPa

S.1.7 Fabrication protocol via Polyjet 3D printing technique

The 3D printed Kresling unit cell fabrication process contemplates three main stages: Design, 3D printing and Post-processing. During the design stage, the 3D CAD parametric models were generated in Autodesk Inventor. The selected geometrical configuration for the experimental validation of the Kresling cells is: C8 case, polygons with n = 6 sides, $\theta_o = \pi/6$, h_o/r=1.75, $t \approx 0.04h_o$, creases width/thickness ratio w/s =1.50 and $RF \leq 0.66$.

The Kresling cell dimensions h_o=17.5 mm and r=10 mm, were scaled three times in order to make feasible their printing and to avoid the dimensional limitations regarding manufacturing. The other geometrical parameters and ratios were maintained to keep the proportions of the analyzed Kresling cells. The parametric design process was previously summarized in Fig. S.22, section S.1.2. The 3D CAD model were saved as Parasolid files ($*.x_b$) to facilitate the exportation of the assembled components in a unique file for 3D printing. At the same time, it enables to identify separately the different components of the Kresling cells, such as panels, peaks, valleys and rings, for the assignation of different materials.

For the printing process, the GrabCAD software was used for the preparation of the printing files to be send to a Stratasys J750 printer series, including automatic slicing. Once the files are imported, the respective dimensions and position along the build tray are controlled. Since the panels were conceived to be made of rigid materials, the VeroBlack photopolymers was selected. In the case of the creases, the following flexible materials were employed in different Kresling cells: AG30, DM60, DM70, DM85 and DM95. The selected support material was SUP706B with the standard grid density mode. It is important to remark that supports were also assigned to the panels during the printing process, because of the presence of inclined faces with respect to the build tray. The printing setting was the following: High-Mix mode with a layer resolution thickness of 27 microns and matte surface finishing.

The post-processing operations include mostly the supports removal, which demands to be meticulously carried on specially considering the small dimensions of the Kresling cells creases being at the edge of Polyjet manufacturing limitation $\leq$ 1.0 mm. The prolonged contact with water or alkaline solutions of small elements and multi-material interfaces lower than 1.0 mm cross-section, lead to a premature breakage and detachment. For this reason, the exposure of the 3D multi-material sample to humidity should be controlled. As an alternative, the support residues were carefully removed mostly by hand and briefly rinsed in water for less than five minutes.

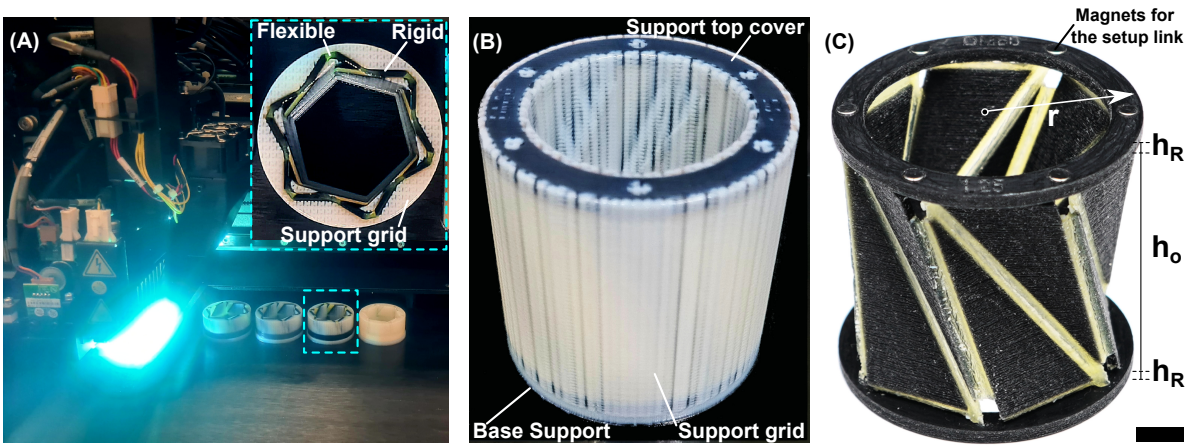

Figure S.9: Fabrication of multi-material Kresling cells. (A) Polyjet printing process and multi-material deposition of rigid (VB), flexible (DM60) and support grid (SUP706B). **(B)** Support material distribution along the samples with matte surface finishing. **(C)** 3D printed Kresling cell from case C8 (RF=0.80) used in the experiments, with the following dimensions: r=30, h_R=3, h_o=52.50, and thickness of the panels $\overline{s}$=2.25. Units: mm. Scale bar: 10 mm.

S.1.8 Experimental setup

A further experimental validation was carried on to involve quasi-static tests on the 3D printed Kresling cells to validate the numerical simulations results. A compression load was applied at the top of the Kresling cell with a Messphysik μ-strain loading frame machine (from ZwickRoell, 0.01 µm stroke measurement resolution). The experiments were performed at a testing speed of 0.1 mm/sec. The applied Load F and displacement u were measured with a AEP TYPE F1-1kN load cell and with a displacement transducer mounted internally to the testing machine, respectively. The tests were stopped once a displacement $u = 1/3h_o$ was applied the sample. The experimental setups, shown in Fig. S.10, consists of two fixtures. The top fixture guarantees free rotation, ϕ, during the folding of the Kresling (allowing the natural twist under compression inherent to Kresling patterns kinematics), while the bottom fixture prevent both displacements and rotations [3].

The free rotational fixture is formed by a rotating plate coupled to a ball bearing (SKF 608 SKF 8x22x7) and a rotational fastener. The Kresling cell samples are directly linked to the top and bottom plates through two different systems. The first one consisted in a female-male connection system used for the Kresling cells with thicker creases, as shown in Fig. S.10A. Pins were created on the surfaces of the samples rings and distributed to coincide with the vertices of the hexagonal polygons. These pins were then inserted into the corresponding holes located in the plates. However, in this system, when using Kresling cells with thinner creases, the samples tended to slide. To prevent this problem, we implemented a second connection system

based on magnets applied to the top and bottom of the samples and the plates, as described in Fig. S.10B. The components of the first setup were 3D printed using the PolyJet technique on a Stratasys J750 3D printer, with tolerances of ±0.2 mm for holes and insertions. In contrast, the second setup was printed using the DLP technique through an Origin-One printer, with tolerances between ±0.1-0.25 mm for the magnet holes and insertions.

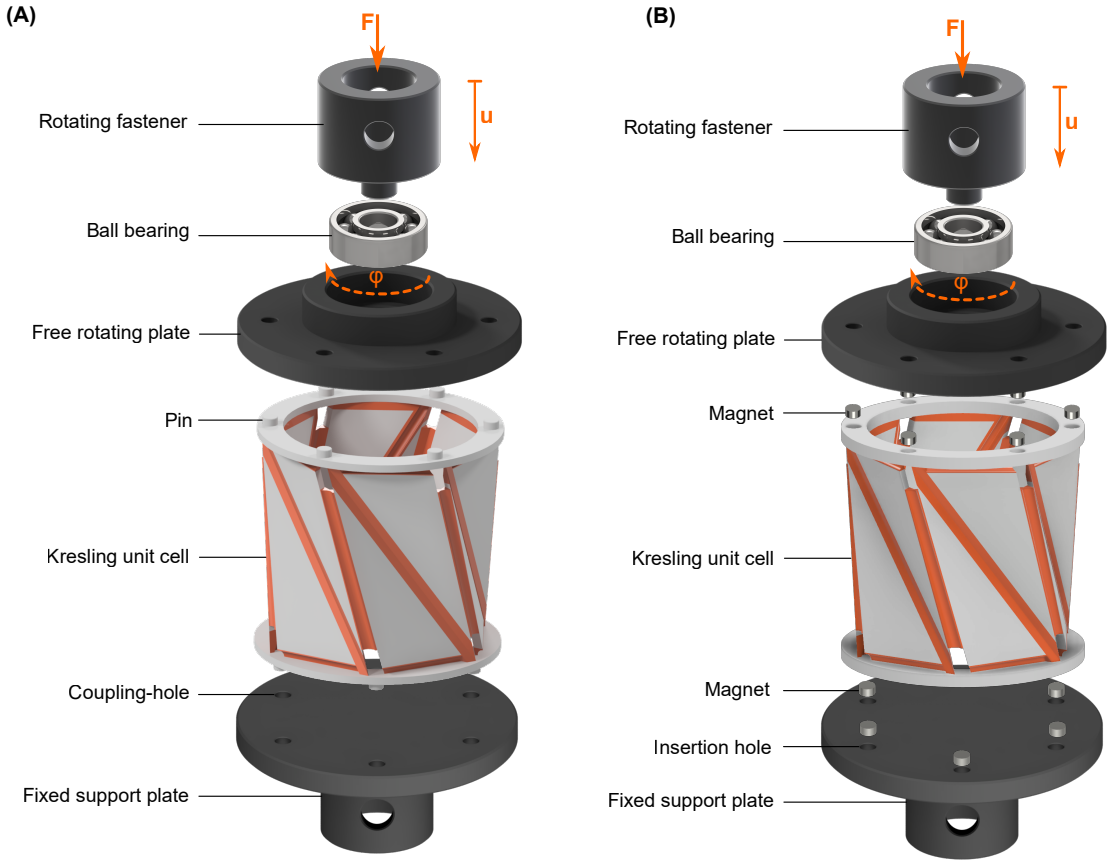

Figure S.10: Experimental setup for compression test with an applied Load F and displacement u. Exploded schemes of the experimental setups with a fixture at the top, enabling a free rotation ϕ, and a fixed support fixture at the bottom with the following connection systems: **(A)** Pins and **(B)** Magnets.

S.1.9 Hands-on experimental validation of Bistability

A manual compressive force was applied to the top of the Kresling cells, allowing free rotation at the top while constraining all displacements and rotations at the bottom. This action enabled us to recreate their spontaneous rotation, reflecting the characteristic kinematics during compression. Thus, we conducted a hands-on validation of bistability to determine which Kresling cells remained in the folded configuration after the manual force was applied. The applied compressive force generated an axial displacement u of approximately one third of the initial height h_o of the Kresling cell.

For example, we compared the behavior of Kresling cells with creases made of the rubbery material DM60 generated with gradual reductions (C8 RF=0.80) versus its corresponding intact creases cell, as shown in Fig. S.11A. We also observed the effects of viscosity in Kresling cells (C8 RF=0.80) with creases made of different rubbery photo-polymers AG30, DM60, DM70, DM85 and DM95, as illustrated in Fig. S.11B. In these hands-on experiments, we confirmed that all Kresling cells with creases generated with RF=0.80 remained in the folded configuration for over 180 seconds after the application of the manual compressive force, thus validating the achieved bistability in the experiments conducted with the testing machine. Conversely, the Kresling cells with creases made of the highly viscous DM95 or the intact cell immediately returned to their original configuration, exhibiting a monostable behavior. The complete hands-on experimental validation is further described in videos S2 and S4.

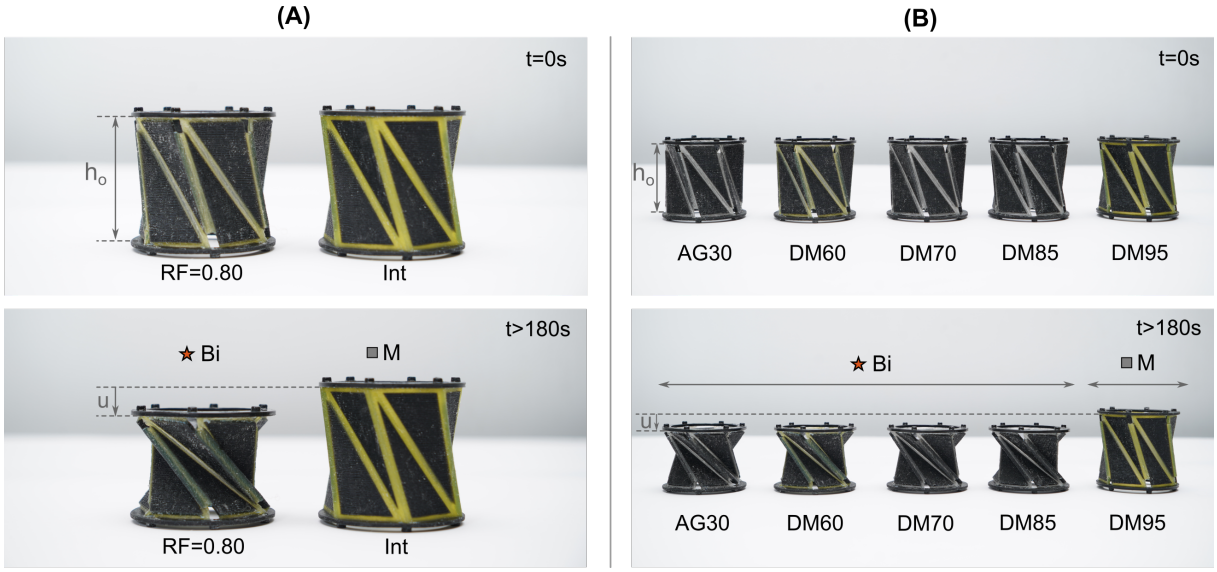

Figure S.11: Hands-on experimental investigation demonstrating the achievement of bistability (Bi) in 3D-printed multi-material Kresling cells of Case 8, by comparing their folding process. **(A)** RF=0.80 versus Intact creases cell (Int). **(B)** Different RF=0.80 cells with creases made of rubbery photopolymers: AG30, DM60, DM70, DM85, and DM95. *Note: The Kresling cells were fabricated with an initial height h_o=52.5 mm, and rigid panels made of VB. The applied force aimed to achieve an axial displacement $u \approx 1/3h_o$.

S.1.10 Microscopic characterization of 3D printed creases results

The dimensional accuracy of the printing process affects the real dimensions of the 3D printed Kresling cells. The measurements of the peaks and valleys creases from the case C8, with gradual reductions between $0.25 \leq RF \leq 0.80$, were analyzed. We established a comparison between those obtained in reality after the Polyjet process and the corresponding exact measurements in the CAD models. A transversal section passing through the half of the Kresling cell was considered to design the sample for the characterization of the geometry of

both types of creases, peaks and valleys. This sample replicates the intermediate substrates of the 3D printed Kresling cell.

The real dimensions of 3D printed samples were determined via a stereo microscope (Nikon SMZ800) equipped with an ED Plan 1.5x lens and with a DS-Ri2 camera. The mean values and the corresponding standard deviations (SD) were obtained from three real measurements (n=3) of the geometrical parameters characterizing the creases, as illustrated in Fig. S.12 and Fig. S.13 for both creases, peaks and valleys. We determined the corresponding mean percentage error, M_{PE} (%) between the dimensions from printed samples (Real) and those used from the CAD models, as follows:

$$M_{PE}(\%) = \frac{100}{n} \sum_{n=1}^{n} \left(\frac{M_{CAD} - M_{Real}}{M_{Real}} \right) \tag{27}$$

The obtained real and exact measurements of the analyzed creases, with the respective M_{PE} (%) error are described in Fig. S.14, in Fig. S.15, Fig. S.16 and Fig. S.17, including peaks and valleys. The measurements taken along the multi-material interface between the rigid and the rubbery photopolymer show differences with an error between $2 \leq M_{PE}$ (%) ≤ 8. The transition zone where the two materials are merging is not homogeneous. For this reason, the dimensions along the edges of the 3D printed creases were not easily measured, potentially leading to an error. Since the internal thickness s_i is a crucial parameter for generating gradual reductions along the creases, we have selected this control parameter to evaluate the impact of differences between the exact and real measurements on the resulting experimental load paths and compare them to the numerical results. Subsequently, an updated CAD model of Kresling cells may be created by adjusting the internal thickness s_i according to the mean real measurements of the analyzed 3D printed creases.

Furthermore, we also observed that when the exact dimensions were designed less than 1.20 mm, the obtained real dimensions in the 3D printing process led to greater values exhibiting a negative error $-1 \leq M_{PE}$ (%) ≤ -25. Specifically, in the cases related to creases with smaller internal thickness s_i generated with the reduction factors ranging within $0.57 \leq RF \leq 0.80$. In contrast, a positive M_{PE} error is achieved when the exact dimensions from the CAD files are above 1.20 mm, such as the cases with reduction factors between $0.25 \leq RF \leq 0.50$. It means that the resulting creases exhibited smaller real dimensions. This fact can be attributed to the printing limitation of fabricating defective load bearing elements with cross-sections around 1 mm, besides the characteristic dimensional accuracy of Polyjet J750 printers. In the case of printing with High-Mix mode, where the layer height reaches 13-16 microns, the exhibited

dimensional accuracy ranges within ±0.06-0.1% for part lengths under ≈100 mm [9], even grasping values around ±0.10 mm in real applications.

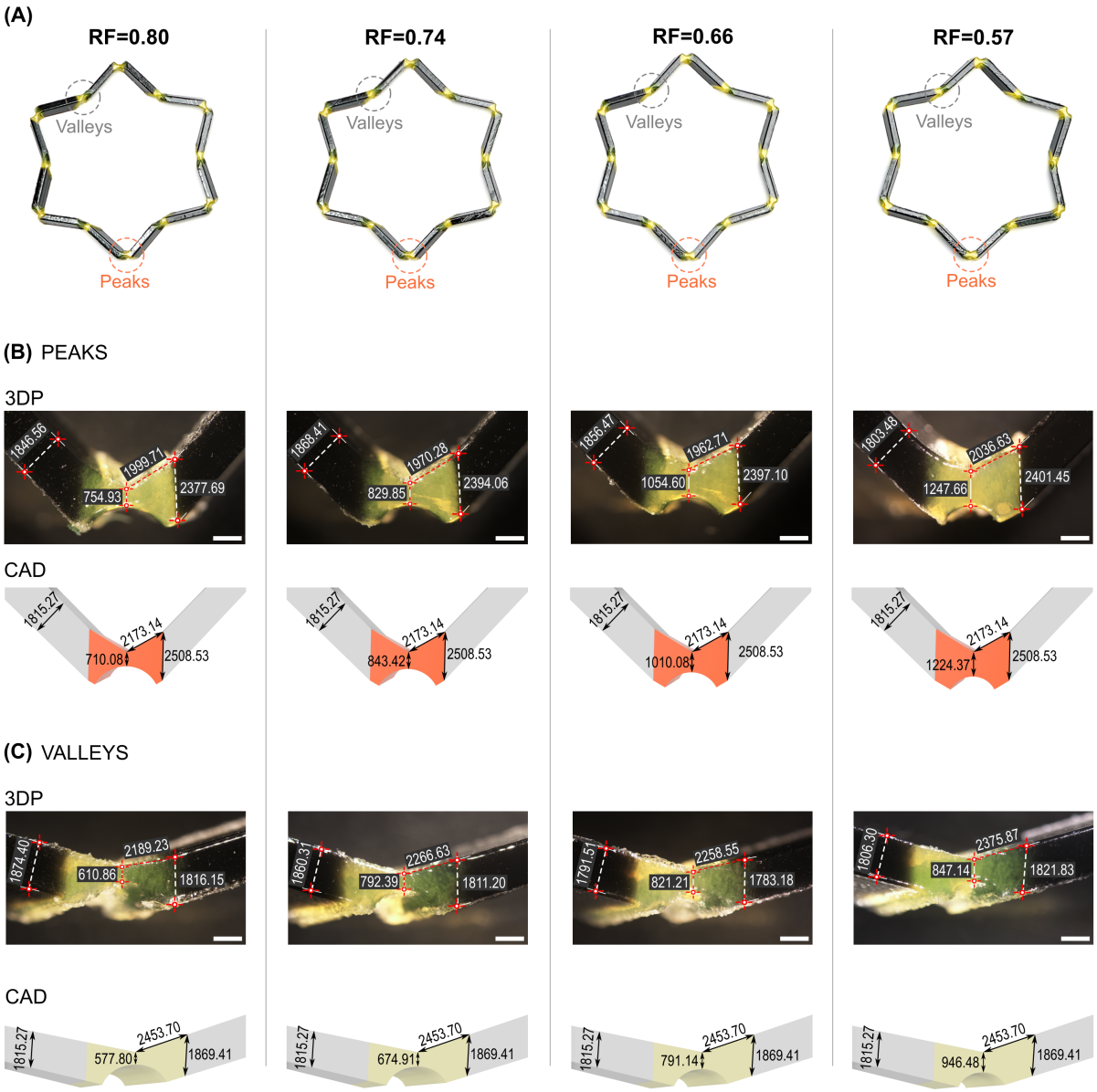

Figure S.12: Microscope characterization of 3D printed creases. **(A)** Intermediate transversal section of the 3D printed Kresling cells from case C8 with gradual reduction factors ranging between $0.57 \leq RF \leq 0.80$ (scale 3:1). Comparison between the real (3DP) and the exact (CAD) measurements of the corresponding: **(B)** Peaks and **(C)** Valleys. Units: microns. Scale bar:1 mm.

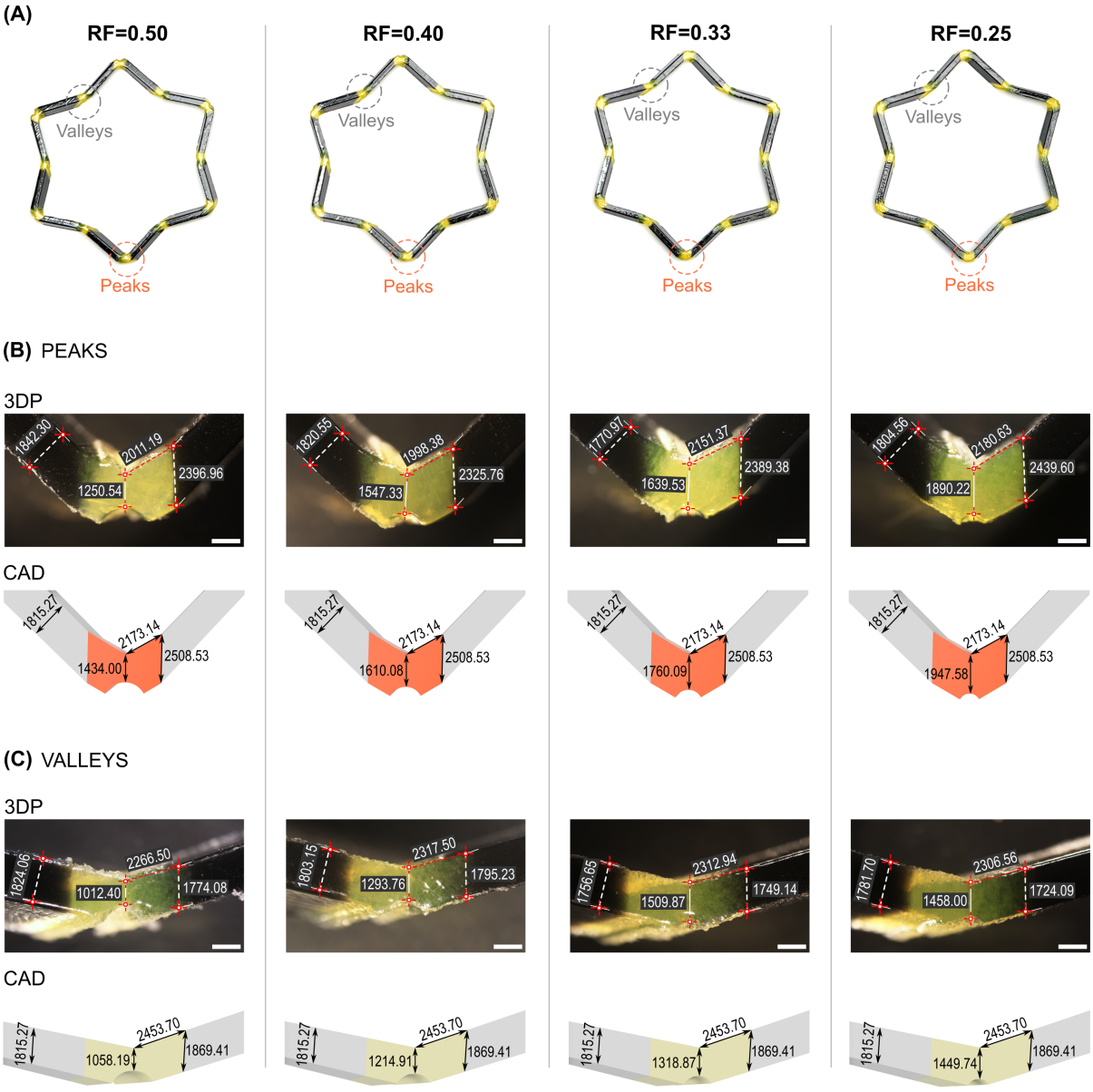

Figure S.13: Microscope characterization of 3D printed creases. **(A)** Intermediate transversal section of the 3D printed Kresling cells from case C8 with gradual reduction factors ranging between $0.25 \leq RF \leq 0.50$ (scale 3:1). Comparison between the real (3DP) and the exact (CAD) measurements of the corresponding: **(B)** Peaks and **(C)** Valleys. Units: microns. Scale bar:1 mm.

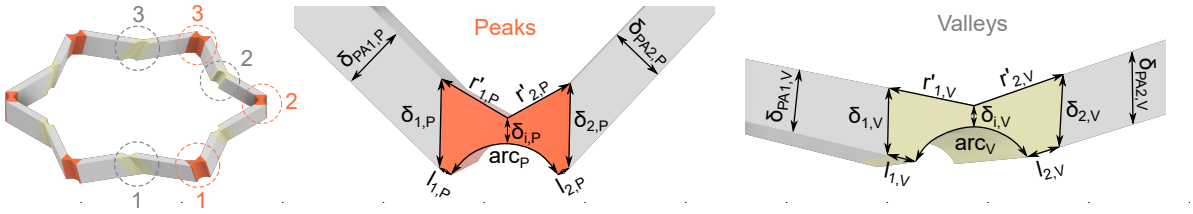

Geometrical Parameters RF=0.80

Peaks measurements

	Meas#	r'1,P	r'2,P	δi,P	δ1,P	δ2,P	δPA1,P	δPA2,P	arcP	l1,P	l2,P
REAL	1	1805.42	1977.77	786.63	2336.39	2323.52	1842.47	1701.28	3843.36	421.35	487.45
	2	2049.90	2123.95	743.41	2567.10	2559.89	1840.53	1753.66	3947.92	335.62	347.94
	3	1797.31	1897.40	734.76	2350.34	2249.66	1856.68	1751.66	3913.40	549.37	538.36
	Mean	1884.21	1999.71	754.93	2417.94	2377.69	1846.56	1735.53	3901.56	435.45	457.92
	SD	143.55	114.86	27.79	129.36	162.05	8.82	29.68	53.28	107.57	98.59
CAD	1	2173.78	2173.14	710.08	2512.84	2508.53	1815.27	1732.96	3773.05	368.96	373.54
	M_{PE} (%)	13.32	7.98	-6.32	3.78	5.22	-1.72	-0.15	-3.41	-18.02	-22.59

Valleys measurements

	Meas#	r'1,V	r'2,V	δi,V	δ1,V	δ2,V	δPA1,V	δPA2,V	arcV	l1,V	l2,V
REAL	1	2095.18	1666.30	639.68	1868.19	1894.55	1851.63	1900.95	3814.28	792.53	656.45
	2	2079.31	1987.27	639.68	1893.64	1732.67	1909.83	1733.86	3800.96	727.67	638.99
	3	2393.20	2258.65	553.23	1876.31	1821.23	1861.73	1793.39	3626.94	986.39	889.77
	Mean	2189.23	1970.74	610.86	1879.38	1816.15	1874.40	1809.40	3747.39	835.53	728.40
	SD	176.82	296.52	49.91	13.00	81.06	31.10	84.69	104.53	134.61	140.02
CAD	1	2453.70	2455.58	577.80	1857.34	1869.41	1815.27	1732.61	3653.10	844.40	824.90
	M_{PE} (%)	10.78	19.74	-5.72	-1.19	2.85	-3.26	-4.43	-2.58	1.05	11.70

Geometrical Parameters RF=0.74

Peaks measurements

	Meas#	r'1,P	r'2,P	δi,P	δ1,P	δ2,P	δPA1,P	δPA2,P	arcP	l1,P	l2,P
REAL	1	2044.80	1999.25	829.85	2481.65	2331.27	1913.83	1727.26	3460.71	448.72	518.83
	2	1956.78	1980.91	829.85	2453.26	2460.88	1864.04	1748.99	3423.04	610.22	702.65
	3	1843.65	1930.68	899.85	2406.09	2390.02	1827.35	1756.54	3427.05	609.43	707.45
	Mean	1948.41	1970.28	853.18	2447.00	2394.06	1868.41	1744.26	3436.93	556.12	642.98
	SD	100.84	35.50	40.41	38.17	64.90	43.41	15.20	20.69	93.01	107.54
CAD	1	2173.78	2173.14	843.42	2512.84	2508.53	1815.27	1732.96	3494.55	502.29	506.87
	M_{PE} (%)	10.37	9.33	-1.16	2.62	4.56	-2.93	-0.65	1.65	-10.72	-26.85

Valleys measurements

	Meas#	r'1,V	r'2,V	δi,V	δ1,V	δ2,V	δPA1,V	δPA2,V	arcV	l1,V	l2,V
REAL	1	2064.31	2149.35	899.01	1870.29	1712.57	1885.14	1682.04	3703.44	877.00	801.23
	2	2457.63	2458.85	622.39	1894.36	1911.09	1839.71	1799.86	3562.02	872.50	885.46
	3	2277.95	2257.50	855.78	1962.17	1809.93	1856.07	1739.69	3725.26	899.96	807.23
	Mean	2266.63	2288.57	792.39	1908.94	1811.20	1860.31	1740.53	3663.57	883.15	831.31
	SD	196.90	157.07	148.81	47.64	99.27	23.01	58.91	88.62	14.73	46.99
CAD	1	2453.70	2455.58	674.91	1857.34	1869.41	1815.27	1732.61	3652.71	958.31	940.19
	M_{PE} (%)	7.62	6.80	-17.41	-2.78	3.11	-2.48	-0.46	-0.30	7.84	11.58

Figure S.14: Microscope characterization of 3D printed peaks and valleys from case C8 (scale 3:1) with 0.74 ≤ RF ≤ 0.80. Mean values, and standard deviation (SD) of the real measurements, besides the mean percentage error $M_{PE}(\%)$ with respect to the exact (CAD) measurements. Units: microns.

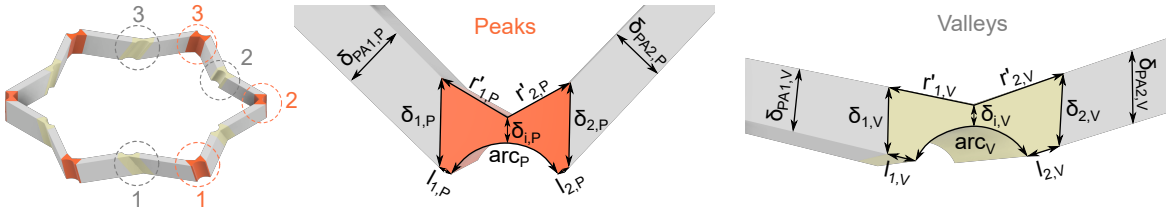

Geometrical Parameters RF=0.66

Peaks measurements

	Meas#	r'1,P	r'2,P	δi,P	δ1,P	δ2,P	δPA1,P	δPA2,P	arcP	l1,P	l2,P
REAL	1	1925.05	1952.67	1089.18	2355.76	2441.13	1882.14	1701.58	3306.21	592.87	661.01
	2	1762.63	1897.89	1097.82	2367.57	2346.68	1840.89	1818.57	3144.04	656.89	707.30
	3	2076.20	2037.56	976.80	2358.92	2403.50	1846.38	1773.73	2918.37	746.48	754.29
	Mean	1921.29	1962.71	1054.60	2360.75	2397.10	1856.47	1764.63	3122.87	665.41	707.53
	SD	156.82	70.37	67.52	6.11	47.55	22.40	59.02	194.78	77.16	46.64
CAD	1	2173.78	2173.14	843.42	2512.84	2508.53	1815.27	1732.96	3494.55	502.29	506.87
	M_{PE} (%)	11.61	9.68	-25.04	6.05	4.44	-2.27	-1.83	10.64	-32.48	-39.59

Valleys measurements

	Meas#	r'1,V	r'2,V	δi,V	δ1,V	δ2,V	δPA1,V	δPA2,V	arcV	l1,V	l2,V
REAL	1	2276.31	2216.95	812.56	1870.04	1810.70	1858.39	1766.07	3234.99	987.65	735.99
	2	2200.04	2255.46	924.94	1816.62	1842.53	1738.40	1790.08	3205.89	914.09	880.13
	3	2299.29	2135.98	726.12	1771.06	1696.32	1777.74	1736.65	3083.61	1163.36	1060.41
	Mean	2258.55	2202.80	821.21	1819.24	1783.18	1791.51	1764.27	3174.83	1021.70	892.18
	SD	51.95	60.98	99.69	49.54	76.89	61.17	26.76	80.33	128.08	162.55
CAD	1	2453.70	2455.58	791.14	1857.33	1869.41	1815.27	1732.61	3044.68	1100.72	1084.35
	M_{PE} (%)	7.95	10.29	-3.80	2.05	4.61	1.31	-1.83	-4.27	7.18	17.72

Geometrical Parameters RF=0.57

Peaks measurements

	Meas#	r'1,P	r'2,P	δi,P	δ1,P	δ2,P	δPA1,P	δPA2,P	arcP	l1,P	l2,P
REAL	1	1843.58	1878.57	1262.07	2383.19	2311.19	1788.05	1730.54	2845.25	843.64	920.16
	2	1951.89	2039.94	1244.78	2474.39	2412.00	1804.26	1770.34	2813.76	815.30	898.31
	3	2072.20	2191.38	1236.13	2409.32	2481.15	1818.14	1762.74	2531.63	910.13	947.11
	Mean	1955.89	2036.63	1247.66	2422.30	2401.45	1803.48	1754.54	2730.21	856.36	921.86
	SD	114.36	156.43	13.21	46.97	85.47	15.06	21.13	172.70	48.68	24.44
CAD	1	2173.78	2173.14	1224.37	2512.84	2508.53	1815.27	1732.96	2697.78	883.24	887.84
	M_{PE} (%)	10.02	6.28	-1.90	3.60	4.27	0.65	-1.25	-1.20	3.04	-3.83

Valleys measurements

	Meas#	r'1,V	r'2,V	δi,V	δ1,V	δ2,V	δPA1,V	δPA2,V	arcV	l1,V	l2,V
REAL	1	2430.01	2413.36	847.14	1888.91	1806.66	1823.66	1801.08	2723.95	1423.84	1265.66
	2	2266.27	2237.62	847.14	1888.21	1807.67	1846.33	1794.40	2855.89	1149.21	1090.58
	3	2438.34	2431.34	838.50	1886.06	1764.47	1839.21	1766.05	2811.48	1354.00	1246.38
	Mean	2378.21	2360.77	844.26	1887.73	1792.93	1836.40	1787.18	2797.11	1309.02	1200.87
	SD	97.03	107.03	4.99	1.49	24.66	11.59	18.60	67.13	142.73	96.00
CAD	1	2453.70	2455.58	946.48	1857.34	1869.41	1815.27	1732.61	2609.96	1283.88	1269.77
	M_{PE} (%)	3.08	3.86	10.80	-1.64	4.09	-1.16	-3.15	-7.17	-1.96	5.43

Figure S.15: Microscope characterization of 3D printed peaks and valleys from case C8 (scale 3:1) with 0.57 $\leq RF \leq$ 0.66. Mean values, and standard deviation (SD) of the real measurements, besides the mean percentage error $M_{PE}(\%)$ with respect to the exact (CAD) measurements. Units: microns.

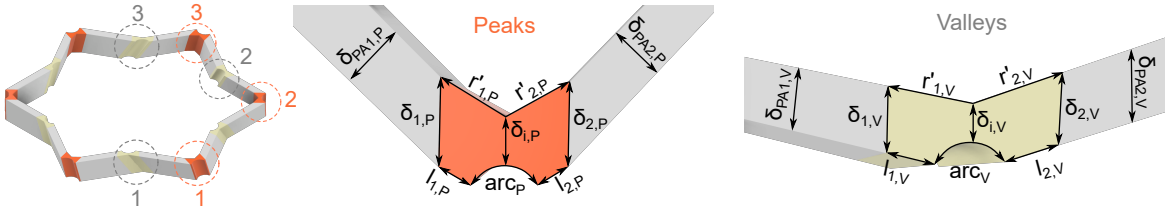

Geometrical Parameters RF=0.50

Peaks measurements

	Meas#	r'1,P	r'2,P	δi,P	δ1,P	δ2,P	δPA1,P	δPA2,P	arcP	l1,P	l2,P
REAL	1	1938.23	1904.66	1296.64	2318.11	2340.35	1784.59	1781.64	2361.64	987.28	1017.38
	2	1975.79	2093.31	1297.49	2412.80	2448.53	1837.37	1773.89	2472.90	978.77	1082.89
	3	2038.33	2035.59	1327.49	2436.15	2402.00	1904.94	1810.34	2531.46	942.40	1078.77
	Mean	1984.12	2011.19	1307.21	2389.02	2396.96	1842.30	1788.62	2455.33	969.48	1059.68
	SD	50.57	96.66	17.57	62.51	54.27	60.33	19.20	86.26	23.84	36.69
CAD	1	2173.78	2173.14	1434.00	2512.84	2508.53	1815.27	1732.95	2361.35	1043.96	1048.55
	M_{PE} (%)	8.72	7.45	8.84	4.93	4.45	-1.49	-3.21	-3.98	7.13	-1.06

Valleys measurements

	Meas#	r'1,V	r'2,V	δi,V	δ1,V	δ2,V	δPA1,V	δPA2,V	arcV	l1,V	l2,V
REAL	1	2322.80	2075.29	985.45	1767.51	1769.52	1807.56	1783.69	2401.85	1563.69	1661.65
	2	2324.10	2312.17	1100.89	1826.11	1806.05	1837.07	1812.26	2260.21	1538.72	1469.46
	3	2152.60	2078.57	950.87	1866.78	1746.68	1827.55	1724.35	2407.22	1193.45	1197.10
	Mean	2266.50	2155.34	1012.40	1820.13	1774.08	1824.06	1773.43	2356.43	1431.95	1442.74
	SD	98.64	135.83	78.56	49.90	29.95	15.06	44.84	83.37	206.93	233.43
CAD	1	2453.70	2455.58	1058.19	1857.34	1869.41	1815.27	1732.61	2283.87	1421.29	1408.90
	M_{PE} (%)	7.63	12.23	4.33	2.00	5.10	-0.48	-2.36	-3.18	-0.75	-2.40

Geometrical Parameters RF=0.40

Peaks measurements

	Meas#	r'1,P	r'2,P	δi,P	δ1,P	δ2,P	δPA1,P	δPA2,P	arcP	l1,P	l2,P
REAL	1	1825.07	1936.91	1547.33	2324.26	2263.44	1799.77	1714.02	2053.97	1205.87	1207.09
	2	2018.29	2079.35	1538.68	2382.63	2377.57	1818.97	1730.74	2040.43	1236.40	1260.02
	3	1992.82	1978.89	1555.97	2281.62	2336.26	1842.91	1790.18	1869.76	1337.59	1353.99
	Mean	1945.39	1998.38	1547.33	2329.50	2325.76	1820.55	1744.98	1988.05	1259.95	1273.70
	SD	104.98	73.19	8.65	50.71	57.79	21.61	40.03	102.67	68.95	74.40
CAD	1	2173.78	2173.14	1610.08	2512.84	2508.53	1815.27	1732.96	1889.97	1268.96	1273.56
	M_{PE} (%)	10.51	8.04	3.90	7.30	7.29	-0.29	-0.69	-5.19	0.71	-0.01

Valleys measurements

	Meas#	r'1,V	r'2,V	δi,V	δ1,V	δ2,V	δPA1,V	δPA2,V	arcV	l1,V	l2,V
REAL	1	2408.36	2429.37	1296.64	1822.79	1793.45	1820.92	1740.57	2044.27	1532.16	1569.42
	2	2276.83	2280.70	1262.07	1798.03	1792.89	1799.84	1740.85	1797.87	1433.65	1416.88
	3	2267.32	2228.39	1322.58	1807.67	1799.34	1788.70	1746.69	1589.70	1479.77	1414.80
	Mean	2317.50	2312.82	1293.76	1809.50	1795.23	1803.15	1742.70	1810.61	1481.86	1467.03
	SD	78.83	104.27	30.36	12.48	3.57	16.36	3.46	227.55	49.29	88.68
CAD	1	2453.70	2455.58	1214.91	1857.34	1869.41	1815.27	1732.61	1827.24	1613.72	1603.74
	M_{PE} (%)	5.55	5.81	-6.49	2.58	3.97	0.67	-0.58	0.91	8.17	8.52

Figure S.16: Microscope characterization of 3D printed peaks and valleys from case C8 (scale 3:1) with 0.40 ≤ RF ≤0.50. Mean values, and standard deviation (SD) of the real measurements, besides the mean percentage error $M_{PE}(\%)$ with respect to the exact (CAD) measurements. Units: microns.

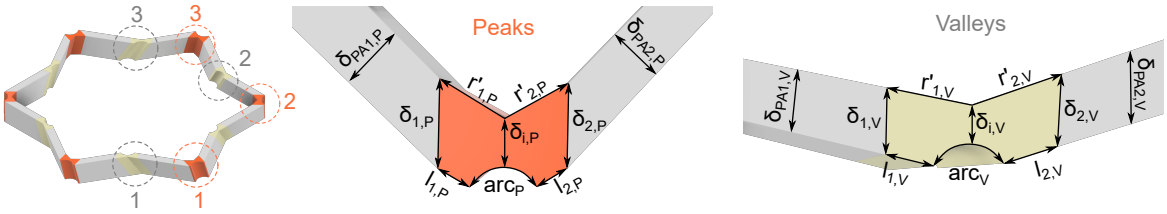

Geometrical Parameters RF=0.33

Peaks measurements

	Meas#	r'1,P	r'2,P	δi,P	δ1,P	δ2,P	δPA1,P	δPA2,P	arcP	l1,P	l2,P
REAL	1	2007.90	2155.04	1590.55	2333.07	2430.29	1859.66	1726.92	1846.22	1322.36	1490.03
	2	2028.15	2180.96	1694.28	2323.11	2403.11	1828.61	1707.10	1693.91	1380.78	1442.26
	3	2092.83	2118.11	1633.77	2312.08	2334.74	1848.64	1697.99	1580.72	1468.83	1542.94
	Mean	2042.96	2151.37	1639.53	2322.75	2389.38	1845.64	1710.67	1706.95	1390.66	1491.74
	SD	44.36	31.59	52.10	10.50	49.23	15.74	14.79	133.23	73.73	50.36
CAD	1	2173.78	2173.14	1760.09	2512.84	2508.53	1815.27	1732.96	1575.47	1418.96	1423.56
	MPE (%)	6.02	1.00	6.85	7.56	4.75	-1.67	1.29	-8.35	1.99	-4.79

Valleys measurements

	Meas#	r'1,V	r'2,V	δi,V	δ1,V	δ2,V	δPA1,V	δPA2,V	arcV	l1,V	l2,V
REAL	1	2342.48	2213.98	1495.46	1748.28	1824.03	1720.14	1731.25	1467.53	1701.94	1518.26
	2	2245.91	2181.91	1538.68	1837.17	1711.47	1798.85	1711.47	1433.87	1951.36	1710.22
	3	2350.44	2343.54	1495.46	1730.69	1711.92	1750.96	1664.61	1075.60	1941.09	1873.85
	Mean	2312.94	2246.48	1509.87	1772.05	1749.14	1756.65	1702.44	1325.67	1864.80	1700.78
	SD	58.19	85.58	24.95	57.08	64.86	39.66	34.22	217.22	141.13	177.98
CAD	1	2453.70	2455.58	1318.87	1857.34	1869.41	1815.27	1732.61	1522.77	1742.04	1733.69
	MPE (%)	5.74	8.52	-14.48	4.59	6.43	3.23	1.74	12.94	-7.05	1.90

Geometrical Parameters RF=0.25

Peaks measurements

	Meas#	r'1,P	r'2,P	δi,P	δ1,P	δ2,P	δPA1,P	δPA2,P	arcP	l1,P	l2,P
REAL	1	2090.82	2177.36	1970.90	2370.55	2333.97	1846.06	1729.49	805.27	1798.33	1948.19
	2	2136.14	2273.04	1823.94	2385.47	2560.47	1860.38	1773.35	1032.96	1676.56	1690.60
	3	2012.82	2091.49	1875.81	2412.80	2424.35	1807.23	1716.87	1280.27	1580.28	1665.81
	Mean	2079.93	2180.63	1890.22	2389.61	2439.60	1837.89	1739.90	1039.50	1685.06	1768.20
	SD	62.38	90.82	74.53	21.43	114.02	37.50	29.64	237.57	109.27	156.37
CAD	1	2173.78	2173.14	1947.58	2512.84	2508.53	1815.27	1732.96	1182.07	1606.46	1611.07
	MPE (%)	4.32	-0.34	2.95	4.90	2.75	-1.25	-0.40	12.06	-4.89	-9.75

Valleys measurements

	Meas#	r'1,V	r'2,V	δi,V	δ1,V	δ2,V	δPA1,V	δPA2,V	arcV	l1,V	l2,V
REAL	1	2381.80	2225.93	1504.11	1817.79	1776.20	1804.06	1740.32	1346.03	1662.17	1605.54
	2	2244.79	2173.83	1513.93	1691.98	1675.51	1732.54	1718.32	1351.15	1855.47	1924.44
	3	2293.10	2291.09	1555.97	1758.96	1720.56	1808.49	1714.21	1307.83	1803.89	1740.83
	Mean	2306.56	2230.28	1524.67	1756.24	1724.09	1781.70	1724.28	1335.00	1773.84	1756.94
	SD	69.49	58.75	27.55	62.95	50.44	42.63	14.04	23.67	100.09	160.06
CAD	1	2453.70	2455.58	1449.74	1857.33	1869.41	1815.27	1732.61	1142.11	1902.48	1896.18
	MPE (%)	6.00	9.17	-5.17	5.44	7.77	1.85	0.48	-16.89	6.76	7.34

Figure S.17: Microscope characterization of 3D printed peaks and valleys from case C8 (scale 3:1) with 0.25 ≤ RF ≤0.33 Mean values, and standard deviation (SD) of the real measurements, besides the mean percentage error $M_{PE}(\%)$ with respect to the exact (CAD) measurements. Units: microns.

S.2 Supplementary Text

S.2.1 Intact Kresling cell 3D analysis

Based on the initial geometrical configuration that leads to bistability, we parametrically designed the 3D Kresling cells, as further detailed in S.1.2. The analyzed group of intact cases was conformed by Kresling cells with a variable width of the creases. This term is expressed in terms of the width versus thickness ratio, denoted as w/s. Thus, the number of intact cases analyzed ranged within ($0.50 \leq w/s \leq 2.00$) with their respective notation: Int 1 to Int 11, as shown in Fig. S.18A.

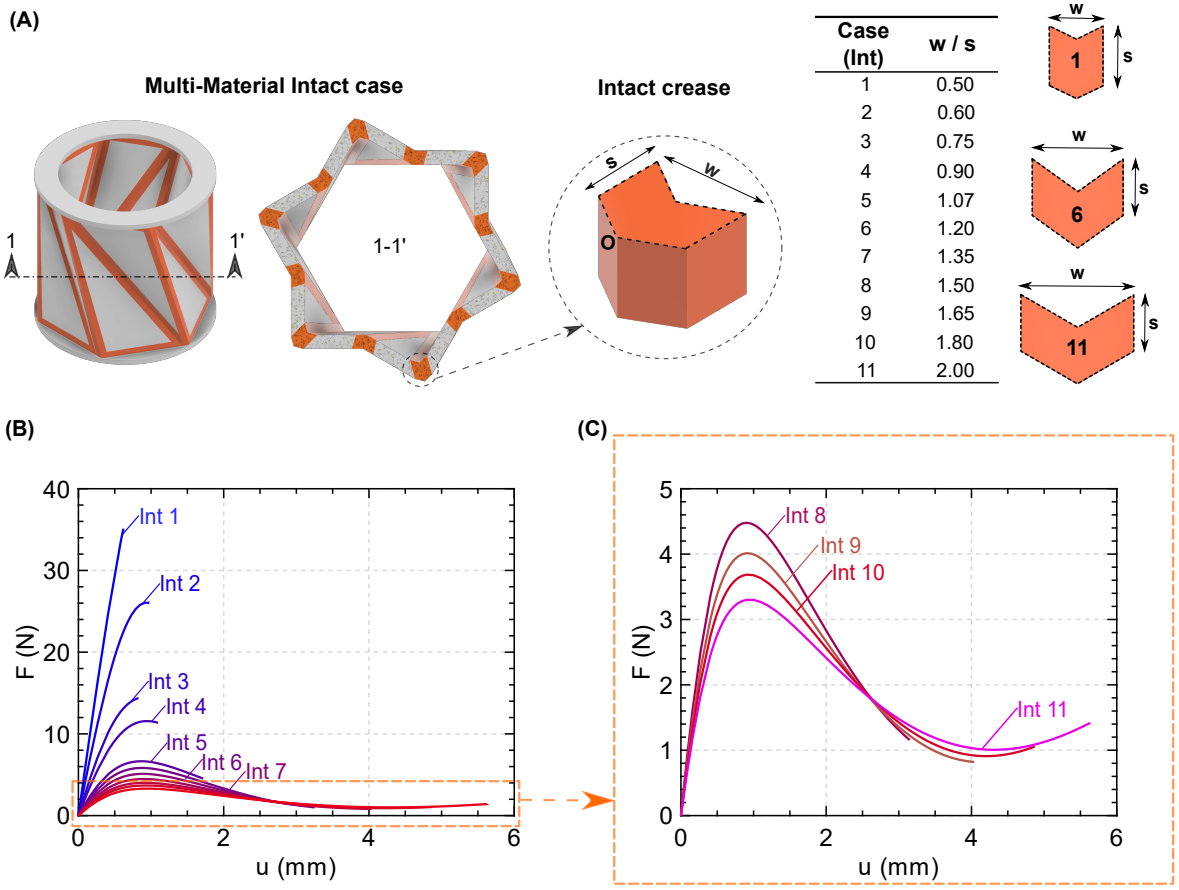

Figure S.18: Kresling cells with intact creases analysis (A) Geometrical details of Intact creases cases, from Int 1 to Int 11, defined in terms of the ratio w/s. Load paths within the ranges: **(B)** $0.50 \leq w/s \leq 2.00$ and **(C)** $1.50 \leq w/s \leq 2.00$.

The load paths obtained from the numerical simulations, depicted in Fig. S.18B, reveal that despite the utilization of flexible creases, the intact cases did not achieved the theoretical bistability as predicted by the preliminary five-parameters model assessment. Specifically, the force values did not reached values below zero, preventing a second local minimum energy state. We have observed that the intact cases with narrower creases (Int 1 to 4) ranging

between ($0.50 \leq w/s \leq 0.90$), tended towards monostability and become highly stiff instead. In contrast, the intact cases (Int 5 to 11) with wider width creases ($1.07 \leq w/s \leq 2.00$), exhibited a monostable behavior. Although using flexible creases facilitates the folding process, the Kresling cell quickly reverts to its initial configuration once the axial load is applied, and second stable state is still not achieved, as evidenced by the load paths in Fig. S.2C. This behavior can be attributed to the restoring force related to the viscoelastic nature of photopolymers. Therefore, these initial results indicate that utilizing elastomeric creases requires further design strategies to potentially achieve a bistable configuration in practice.

S.2.2 Creases design: Complementary results

The parametric study of the Kresling cells with the creases design, results from the numerical simulations in Abaqus/CAE Standard, shown in Fig. S.19. We assessed how the gradual reductions creases affected the energy landscape and the transition form a bistable (Bi) to a monostable (M) behavior. As narrower the internal thickness s_i, the Kresling cell tends to achieve bistability.

This is especially observed in wider creases with a ratio $w/s \geq 1.20$, with an internal thickness s_i and reduction factors between $0.66 \leq RF \leq 0.80$, taking values between $0.1 \leq s_i/s \leq 0.70$. It is evidenced in the load paths with their corresponding stored energy landscapes, U, from Fig. S.20 to Fig. S.23. Moreover, the sequential experiments conducted on the Kresling cells within the range potentially exhibiting bistability ($0.66 \leq RF \leq 0.80$) are presented in Fig. S.24. The results reveal a loss of load capacity of approximately 50% due to the degradation of the thin rubbery creases (RF=0.80). In contrast, thicker creases (RF=0.66) appeared more resistant, losing around 30% of load capacity. The analyzed Kresling cell cases were designed according to the geometrical parameters detailed in Fig. S.25 for a 1:1 scale.

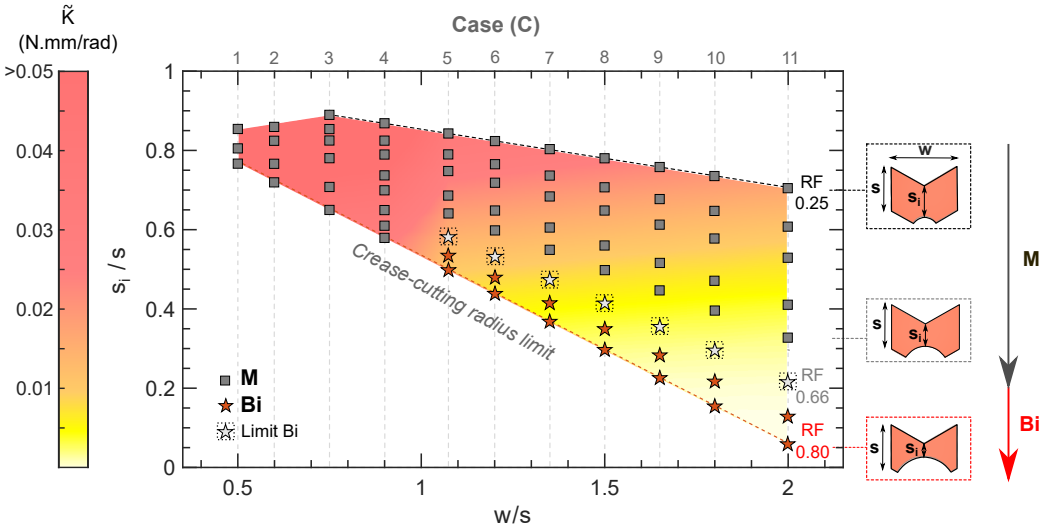

Figure S.19: Parametric study of the creases geometry. Geometrical parameters with their attained Rotational Stiffness ($\tilde{K}$), that lead to monostability (M) or bistability (Bi). 'Limit Bi': boundary between (Bi) and (M) determined experimentally. *The crease edge limit determines the range of reduction radius factors, RF, to maintain a Circular shape at the lower part of the crease. Results from Kresling cells at 1:1 scale.

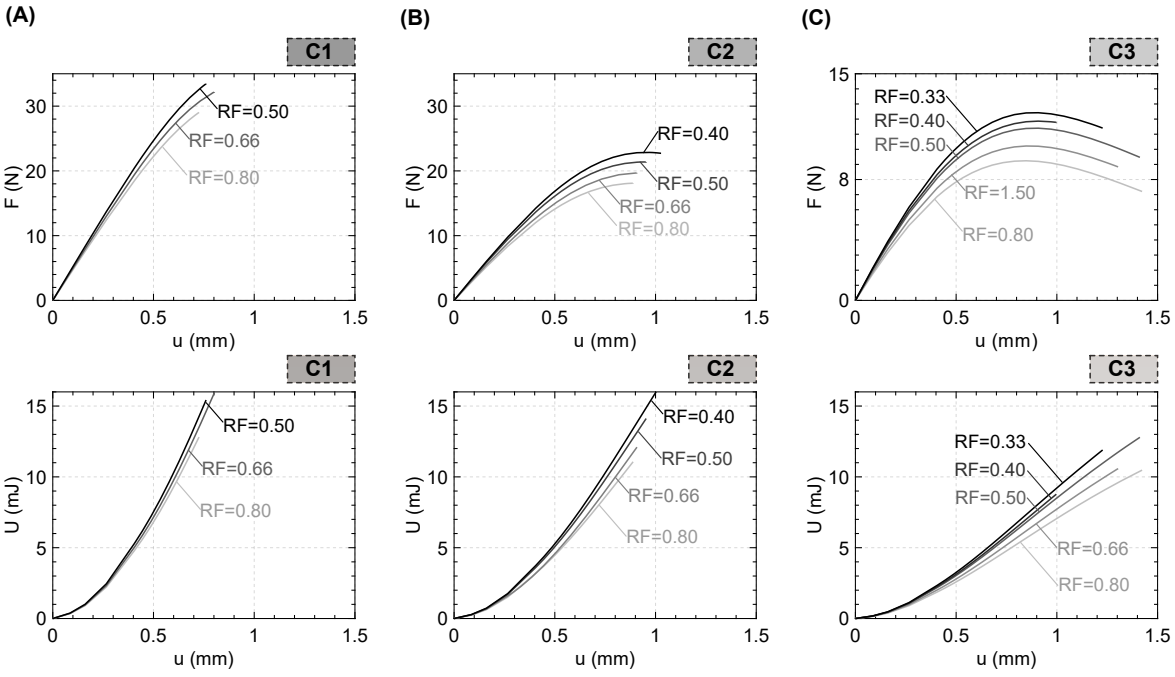

Figure S.20: Load paths and stored energy (U) landscapes variation according to the crease internal thickness (s_i) decrement based on the reduction factors RF. (A) C1 (w/s = 0.50), **(B)** C2 (w/s = 0.60) and **(C)** C3 (w/s = 0.75). The corresponding curves were generated until the panels started to be in contact during the numerical simulations.

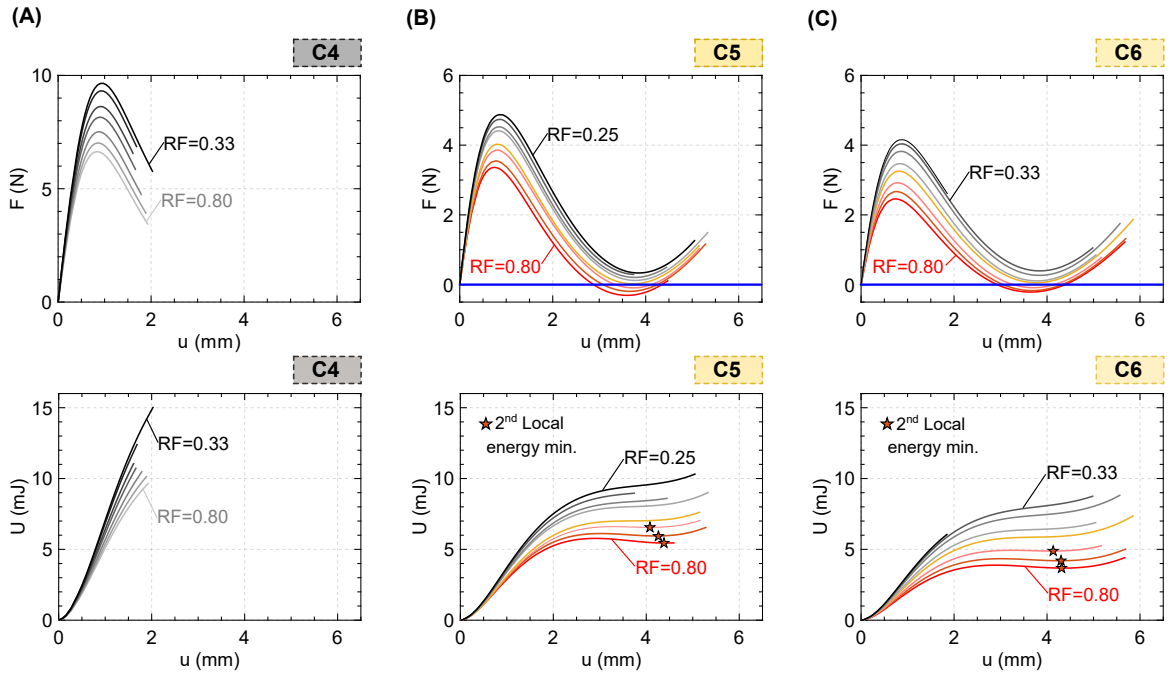

Figure S.21: Load paths and stored energy (U) landscapes variation according to the reduction factors RF. (A) C4 (w/s = 0.90), **(B)** C5 (w/s = 1.07), and **(C)** C6 (w/s = 1.20). The corresponding curves are presented in the following order RF: 0.25, 0.33, 0.40, 0.50, 0.57, 0.66, 0.74, and 0.80.

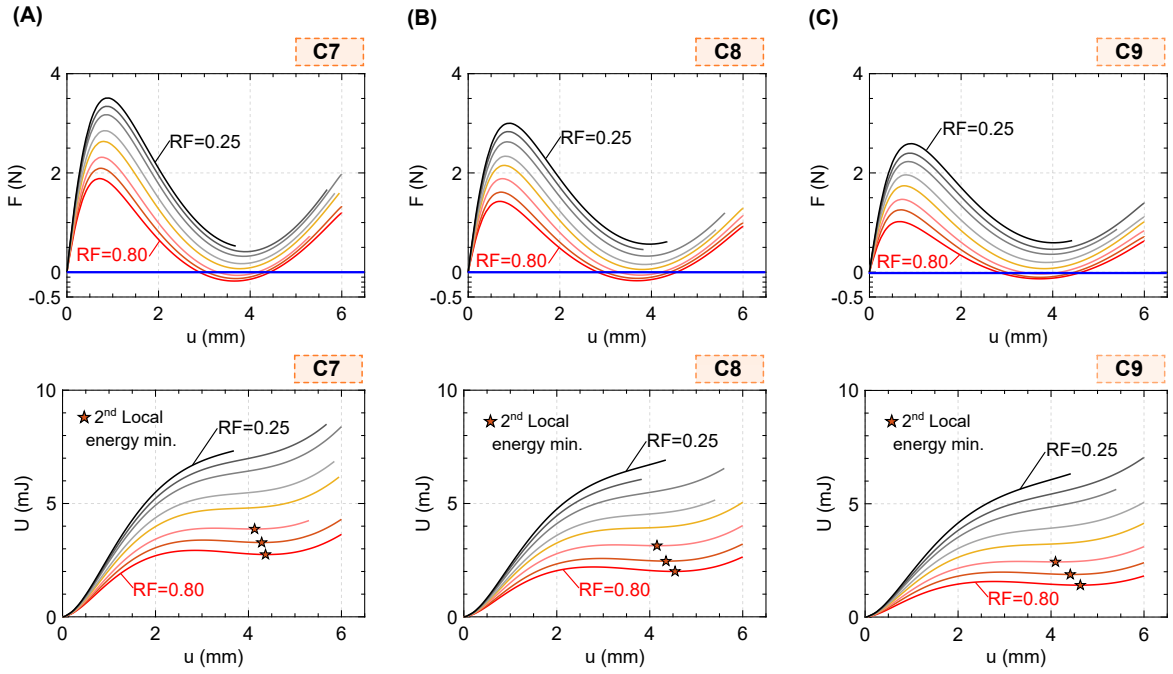

Figure S.22: Load paths and stored energy (U) landscapes variation according to the reduction factors RF. (A) C7 (w/s = 1.35), **(B)** C8 (w/s = 1.50) and **(C)** C9 (w/s = 1.65). The corresponding curves are presented in the following order RF: 0.25, 0.33, 0.40, 0.50, 0.57, 0.66, 0.74, and 0.80.

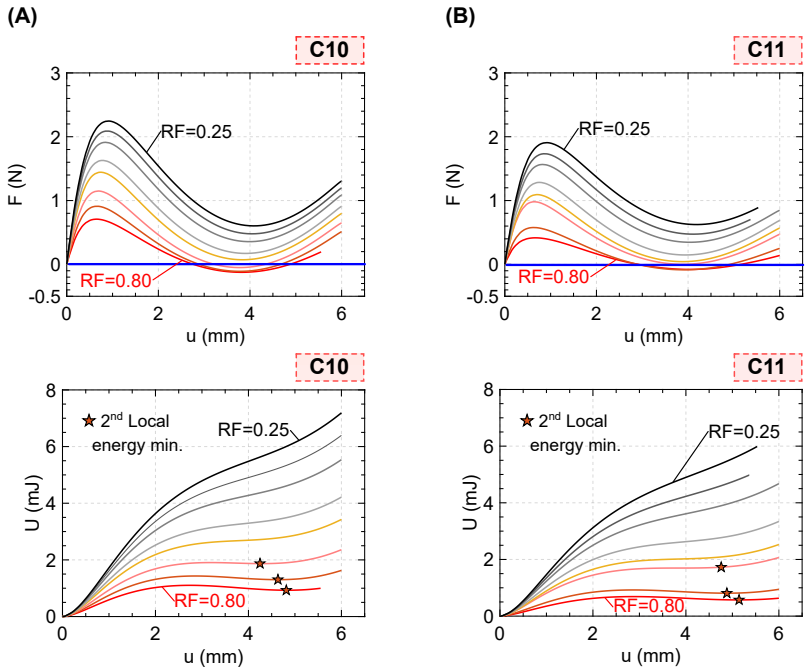

Figure S.23: Load paths and stored energy (U) landscapes variation according to the reduction factors. **(A)** C10 (w/s = 1.80), and **(B)** C11 (w/s = 2.00). The corresponding curves are presented in the following order RF: 0.80, 0.74, 0.66, 0.57, 0.50, 0.40, 0.33, and 0.25.

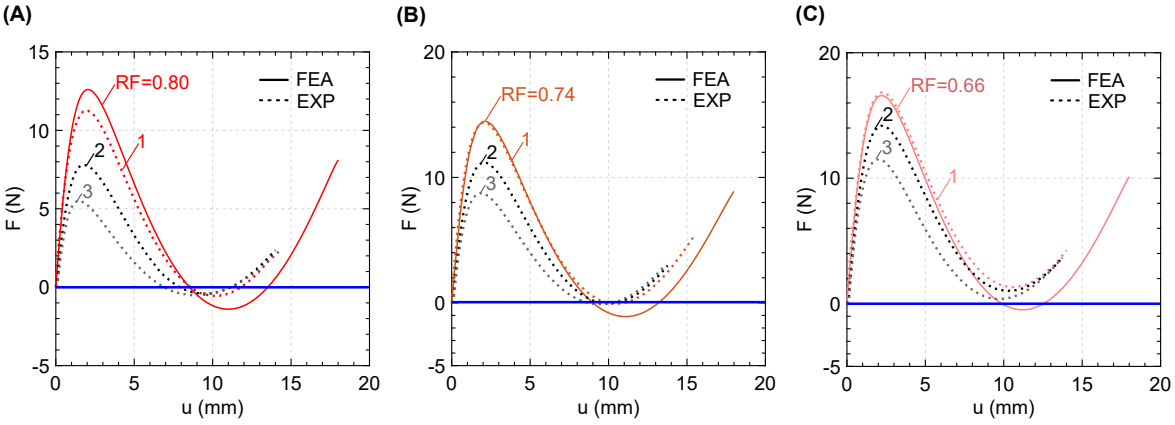

Figure S.24: Effect of the degradation of the rubbery crease cross- sections on the load path after performing sequential experiments on the same samples. **(A)** RF=0.80, **(B)** RF=0.74 and **(C)** RF=0.66. Kresling cells case C8 fabricated with creases made of DM60, at 3:1 scale.

Geometrical Parameters							
Case #	w/s	s	r'	RF	s_c	s_i	s_i/s
1	0.50	1.71	1.00	0.80	0.80	1.31	0.77
				0.66	0.66	1.38	0.81
				0.50	0.50	1.46	0.85
2	0.60	1.43	1.00	0.80	0.80	1.03	0.72
				0.66	0.66	1.10	0.77
				0.50	0.50	1.18	0.82
				0.40	0.40	1.23	0.86
3	0.75	1.14	1.00	0.80	0.80	0.74	0.65
				0.66	0.66	0.81	0.71
				0.50	0.50	0.89	0.78
				0.40	0.40	0.94	0.83
				0.33	0.33	0.98	0.85
				0.25	0.25	1.02	0.89
4	0.90	1.14	1.20	0.80	0.96	0.66	0.58
				0.74	0.89	0.70	0.61
				0.66	0.79	0.74	0.65
				0.57	0.68	0.80	0.70
				0.50	0.60	0.84	0.74
				0.40	0.48	0.90	0.79
				0.33	0.40	0.94	0.82
				0.25	0.30	0.99	0.87
5	1.07	0.86	1.08	0.80	0.86	0.43	0.50
				0.74	0.80	0.46	0.53
				0.66	0.71	0.50	0.58
				0.57	0.61	0.55	0.64
				0.50	0.54	0.59	0.69
				0.40	0.43	0.64	0.75
				0.33	0.35	0.68	0.79
				0.25	0.27	0.72	0.84
6	1.20	0.86	1.20	0.80	0.96	0.38	0.44
				0.74	0.89	0.41	0.48
				0.66	0.79	0.46	0.53
				0.57	0.69	0.51	0.60
				0.50	0.60	0.56	0.65
				0.40	0.48	0.62	0.72
				0.33	0.40	0.66	0.77
				0.25	0.30	0.71	0.82
7	1.35	0.85	1.35	0.80	1.08	0.31	0.37
				0.74	1.00	0.35	0.41
				0.66	0.89	0.40	0.47
				0.57	0.77	0.47	0.55
				0.50	0.68	0.52	0.61
				0.40	0.54	0.58	0.68
				0.33	0.45	0.63	0.74
				0.25	0.34	0.69	0.80

Geometrical Parameters							
Case #	w/s	s	r'	RF	s_c	s_i	s_i/s
8	1.50	0.85	1.50	0.80	1.20	0.25	0.30
				0.74	1.11	0.30	0.35
				0.66	0.99	0.35	0.41
				0.57	0.86	0.42	0.50
				0.50	0.75	0.48	0.56
				0.40	0.60	0.55	0.65
				0.33	0.50	0.60	0.71
				0.25	0.38	0.67	0.78
9	1.65	0.85	1.65	0.80	1.32	0.19	0.23
				0.74	1.22	0.24	0.28
				0.66	1.09	0.30	0.35
				0.57	0.94	0.38	0.45
				0.50	0.83	0.44	0.52
				0.40	0.66	0.52	0.61
				0.33	0.54	0.58	0.68
				0.25	0.41	0.65	0.76
10	1.80	0.85	1.80	0.80	1.44	0.13	0.15
				0.74	1.33	0.18	0.22
				0.66	1.19	0.25	0.30
				0.57	1.03	0.34	0.40
				0.50	0.90	0.40	0.47
				0.40	0.72	0.49	0.58
				0.33	0.59	0.55	0.65
				0.25	0.45	0.63	0.74
11	2.00	0.85	2.00	0.80	1.60	0.05	0.06
				0.74	1.48	0.11	0.13
				0.66	1.32	0.18	0.22
				0.57	1.14	0.28	0.33
				0.50	1.00	0.35	0.41
				0.40	0.80	0.45	0.53
				0.33	0.66	0.52	0.61
				0.25	0.50	0.60	0.70

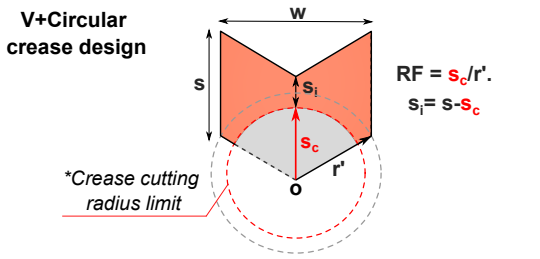

Figure S.25: Geometrical Parameters of creases with gradual reductions. Dimensions taken from the top of the Kresling cells. Units: mm, scale: 1:1.

S.2.3 Estimation of Rotational Stiffness in Creases

Whether a rubbery material is considered for the design of the creases, large deformations are expected to be developed. The V-shape+Circular cross-section of the creases can be simplified into an equivalent rectangular strip that delimits the zone predominantly under bending. Its dimensions are the width w and the internal thickness s_i, where the latter varies according to a reduction factor RF. Thereby, we assessed the effects of the decrement of cross-sections on the rotational stiffness, $\tilde{K}$, of the designed creases. The angular rotation ψ, corresponding to a given bending moment M applied on the equivalent section, can be estimated considering the formulations of bending of a incompressible elastic Neo-Hookean block proposed by [10]. This method assumes that the deformed configuration of the block follows the shape of a planar sector of a cylindrical tube with a thickness s_f, an initial angle ψ_i and a radius $\bar{r}$, as shown in Fig. S.26A. The last two terms define the cylindrical coordinates of the system, thus: $\bar{r}\epsilon[\bar{r}_f, \bar{r}_f + s_f]$ and $\psi\epsilon f[-\psi_i, \psi_i]$, being the out of plane terms neglected. The term $\bar{r}$ can be calculated by fulfilling the impressibility constraint, where the deformed section is equal to the initial area defined by s_i and w. Then, the following relation can be established:

$$\bar{r}_f = \frac{w\ s_i}{2\ \psi_i\ s_f} - \frac{s_f}{2} \tag{28}$$

Considering a Neo-Hookean response of the section, one of the principal stress components T_ψ in cylindrical form is defined as:

$$T_\psi(\bar{r}) = G_o\left(-\frac{w^2}{8\psi_i^2\bar{r}^2} + \frac{6\psi_i^2}{w^2}\bar{r}^2 - 1\right) - \frac{G_o}{2}\left(-\frac{w^2}{4\psi_i^2(\bar{r}_f + s_f)^2} + \frac{4\psi_i^2(\bar{r}_f + s_f)^2}{w^2} - 2\right). \tag{29}$$

where, G_o is the initial shear modulus and the thickness s_f of the deformed configuration can be obtained by the following expression:

$$s_f = \frac{w}{\psi_i\sqrt{2}}\sqrt{-1 + \sqrt{1 + 4\psi_i^2\frac{s_i^2}{w}}} \tag{30}$$

The bending moment M, corresponding to the stress on the deformed configuration, is calculated by the following integration in the interval $[\bar{r}_f, \bar{r}_f + s_f]$:

$$M = \int_{\bar{r}_f}^{\bar{r}_f + s_f} \bar{r}T_\psi(\bar{r})\, d\,\bar{r} \tag{31}$$

Using Eq.31, we calculated the bending moment M of the equivalent cross- sections, M, obtained at a given rotational angle ranging within $0 \leq \psi \leq \pi/2$. The analytical results of the creases from cases C8 (w/s = 1.50) and C11 (w/s = 2.00) were selected for validation against numerical simulations in Abaqus/CAE-Standard, as indicated in Fig. S.26B and C, respectively. The thicknesses of the equivalent rectangular blocks correspond to the variable internal thickness s_i generated by reduction factors ranging from $0.25 \leq RF \leq 0.80$. Moreover, the corresponding mesh was created using biquadratic hybrid elements (CPE8RH). The equivalent rectangular blocks were subjected to bending until reaching a rotational angle of $\psi = \pi/2$ allowing us to obtain the corresponding bending moment M. This demonstrated the close alignment between the FEA calculations and the analytical formulation. Furthermore, the plots from Fig. S.27 depict the bending moment values obtained in Eq.31 at a given rotational angle $0 \leq \psi \leq \pi/2$, applied to the equivalent cross-sections corresponding to crease cases C1 to C11, along with their respective reduction factors RF, as well as the related intact crease cases.

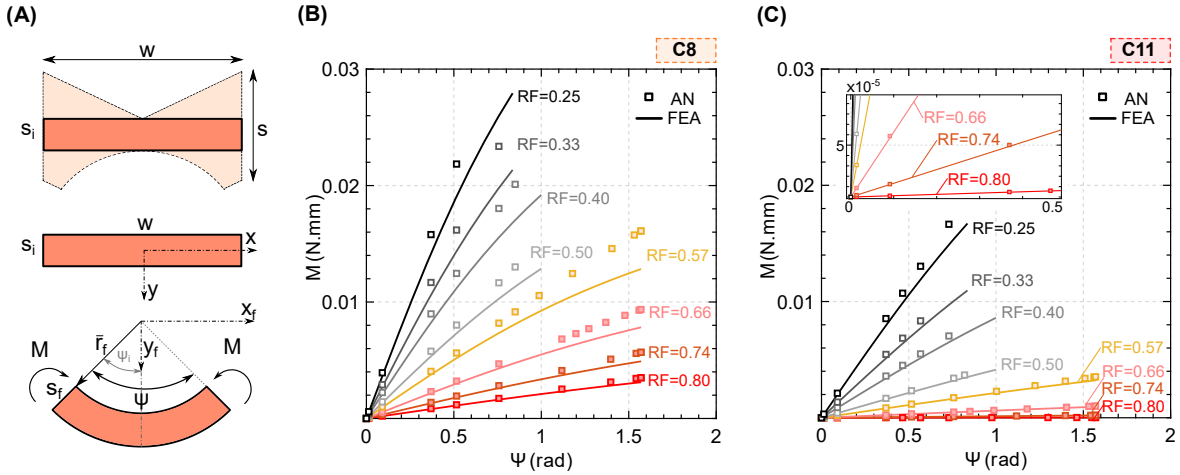

Figure S.26: Rotational stiffness calculation. **(A)** Bending of an incompressible rectangular block equivalent to the crease cross-section. Comparison of analytical and FEA results for the bending moment, M, and angular rotation, ψ, in cases: **(B)** C8 (w/s = 1.50) and **(C)** C11 (w/s = 2.00). *Note: Results are presented in the order reduction factors ranging from $0.25 \leq RF \leq 0.80$, representing a variable s_i

Then, the rotational stiffness was obtained using the expression: $\tilde{K} = M/\psi$. We observed that rotational stiffness depends on the variation of internal thicknesses s_i, their associated reduction factors RF, and the width of the creases w. For instance, bistable creases with thinner internal thicknesses, generated by reduction factors $0.66 \leq RF \leq 0.80$ and ranges of $0.30 \leq s_i/s \leq 0.40$ (C8) and $0.05 \leq s_i/s \leq 0.21$ (C11), achieved the highest angular rotation value $\psi = \pi/2 \approx 1.57$ rad at lower bending moments. Consequently, they exhibited higher flexibility and lower rotational stiffness than their thicker creases counterparts, which fall within the ranges $s_i/s \geq 0.57$ (C8) and $s_i/s \geq 0.37$ (C11), as previously shown in Fig. S.19.

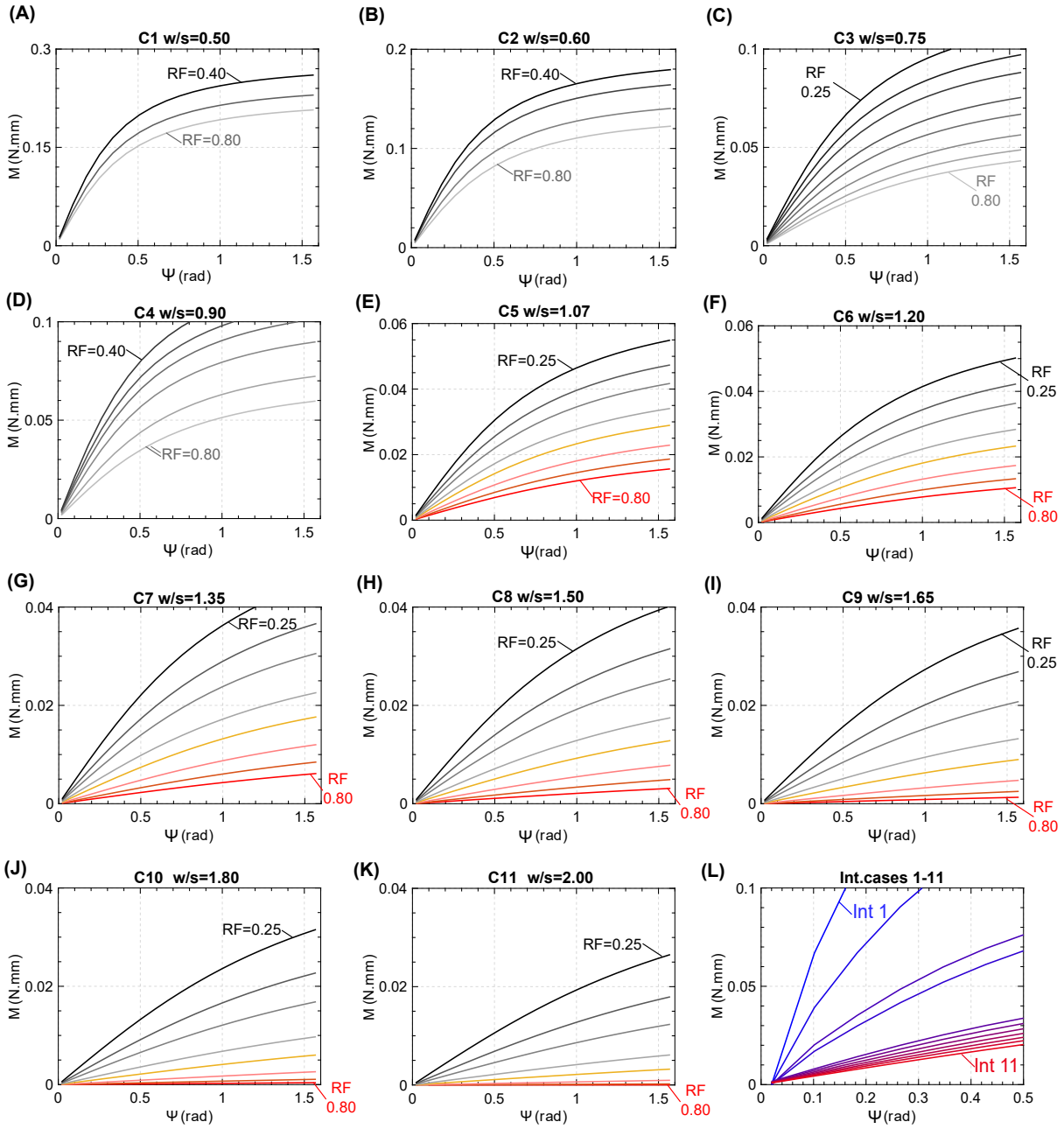

Figure S.27: Bending Moment M versus Rotational angle ψ curves. Calculation obtained from the equivalent cross-sections of the cases C1 (A) to C11 (K), and Intact cases from 1 to 11.

S.2.4 Effects of creases viscosity on bistability: Complementary Results

The assessment of bistability in Kresling cells with creases made from different rubbery materials is presented in Fig. S.28, which is constructed from the load paths and energy landscapes illustrated in Figs. S.29-S.32, based on analyses of Kreling cells at 1:1 scale (x1). We determined whether creases with varying viscosity and relaxation moduli can still achieve bistability, as explored in the parametric study in section 2.1. The numerical simulations were conducted for a time duration corresponding to the limits of the initial (τ_i^*), short- (τ), and long-term ($n\tau$) relaxation regions to predict whether viscosity effects influence the achievement of bistability at different time scales. Moreover, we conducted experiments on Kresling cells (C8 RF=0.80, fabricated at a 3:1 scale) with creases made of AG30, DM60, DM70, DM85, and DM95, as shown in Fig. S.33. An average load capacity loss of approximately 50% was observed due to degradation of the crease cross-sections, with lower peak load decrements in softer photopolymers (AG30, DM60, and DM70) which have lower viscosity and relaxation moduli.

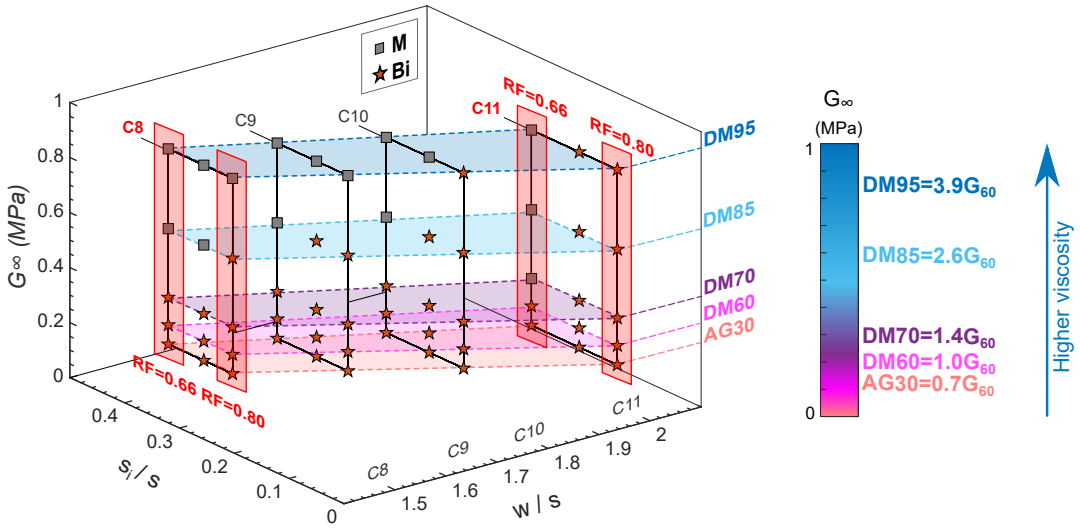

Figure S.28: Visco-hyperelastic effects on bistability. Parametric study assessing the achievement of bistability in creases made of rubbery materials (AG30, DM60, DM70, DM85, and DM95) with varying visco-hyperelastic properties, characterized by relaxation modulus G_∞. Where G_{60} = 0.220 MPa. The study focuses on Cases C8, C9, C10, and C11, designed with reduction factors RF=0.80, RF=0.74 and RF=0.66.

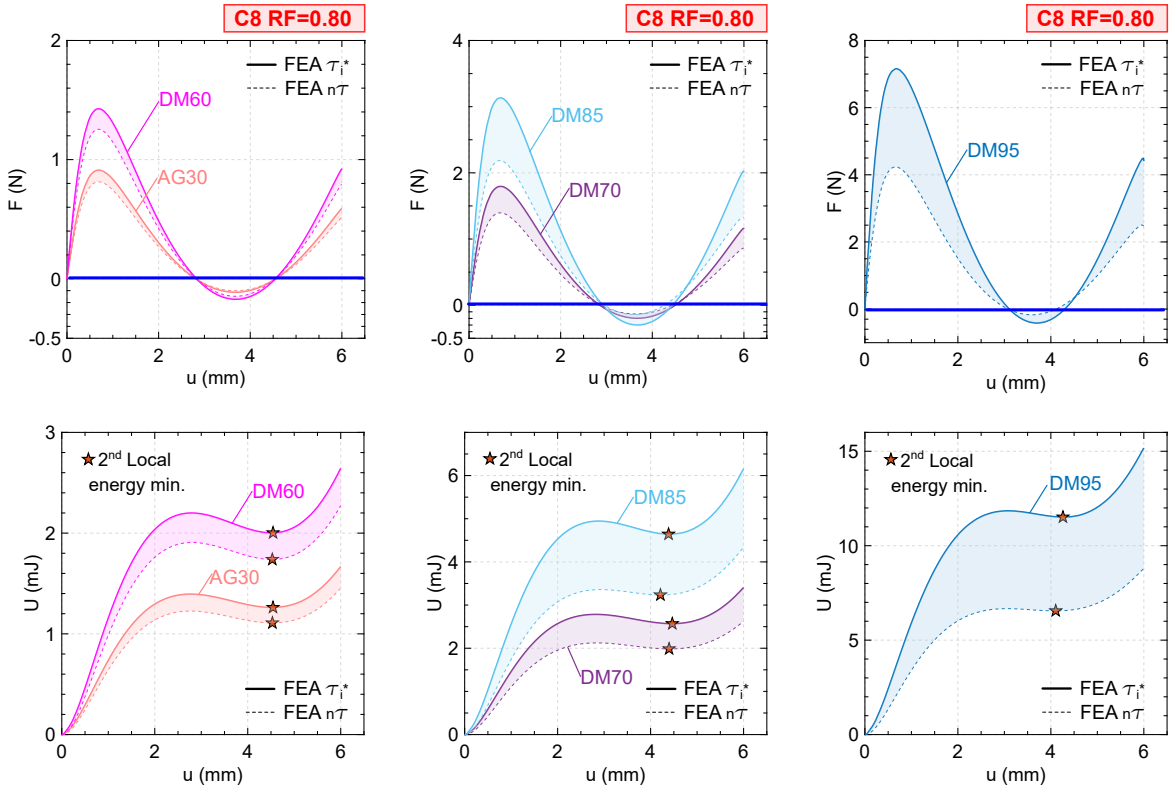

Figure S.29: Load paths and stored energy landscapes of case C8 RF=0.80. Creases: AG30, DM60, DM70, DM85 and DM95. Results for C8 RF=0.80 cells at a 1:1 scale (×1). Filled regions include FEA simulations within the range $\tau_i^* \leq \tau \leq n\tau$.

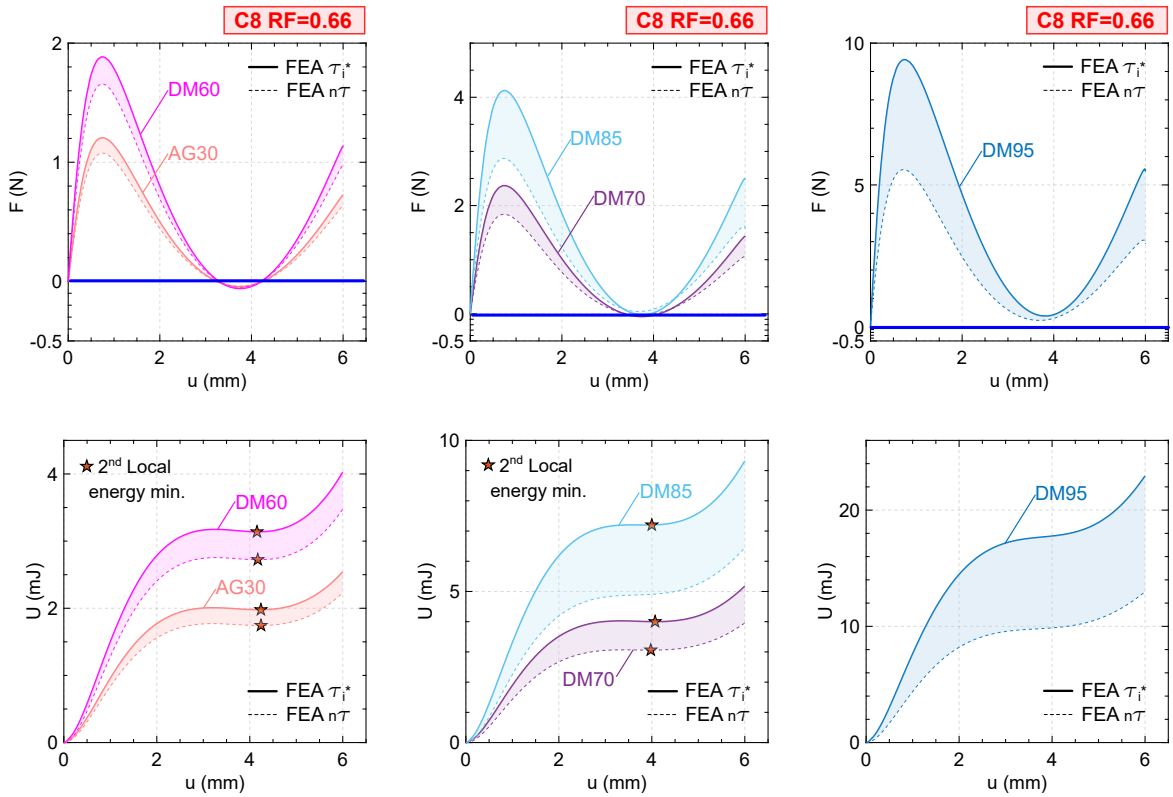

Figure S.30: Load paths and energy landscapes of case C8 RF=0.66. Creases: AG30, DM60, DM70, DM85 and DM95.Results for C8 RF=0.66 cells at a 1:1 scale (×1). Filled regions include FEA simulations within the range $\tau_i^* \leq \tau \leq n\tau$.

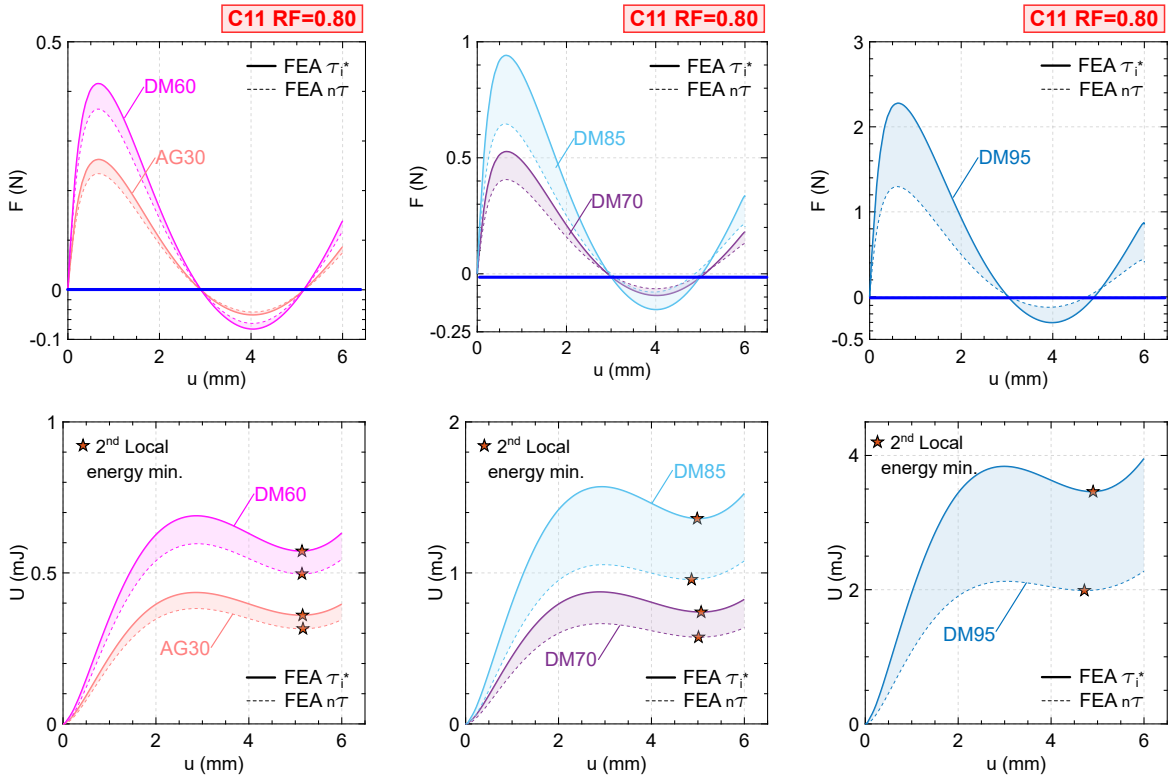

Figure S.31: Load paths and energy landscapes of case C11 RF=0.80. Creases: AG30, DM60, DM70, DM85 and DM95. Results for C11 RF=0.80 cells at a 1:1 scale (×1). Filled regions include FEA simulations within the range $\tau_i^* \leq \tau \leq n\tau$.

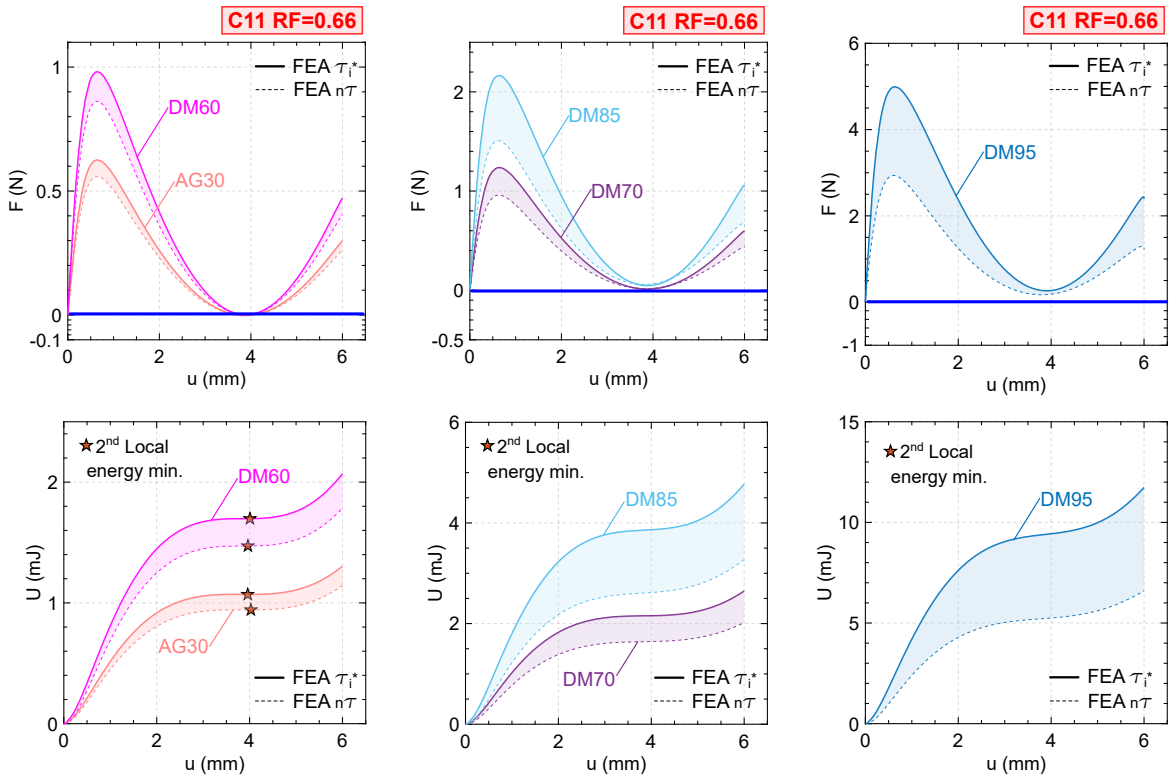

Figure S.32: Load paths and energy landscapes of case C11 RF=0.66. Creases: AG30, DM60, DM70, DM85 and DM95. Results for C11 RF=0.66 cells at a 1:1 scale (×1). Filled regions include FEA simulations within the range $\tau_i^* \leq \tau \leq n\tau$.

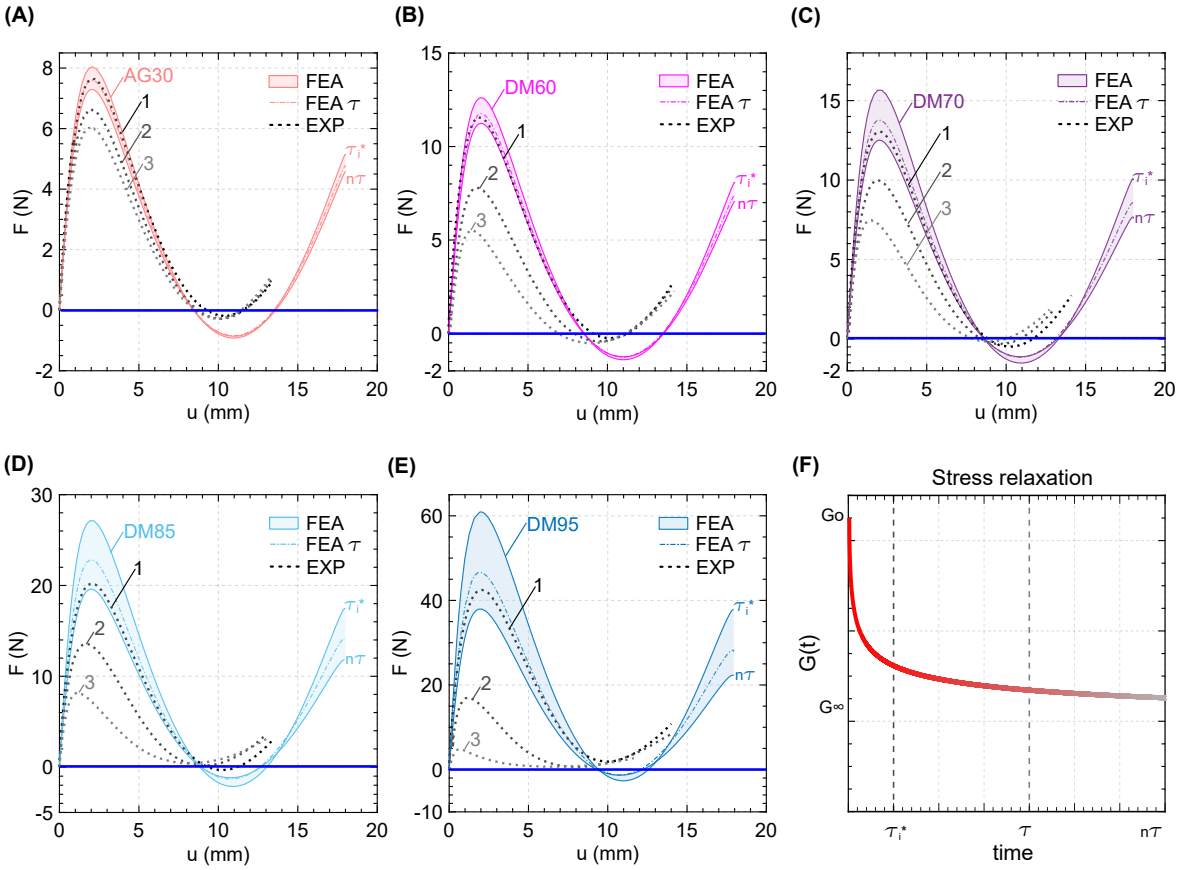

Figure S.33: Effect of the degradation of the rubbery crease cross-sections on the load path. Experimental results after performing three sequential tests on Kresling cells C8 RF=0.80 with creases made of: **(A)** AG30, **(B)** DM60, **(C)** DM70, **(D)** DM85 and **(E)** DM95. Kresling cells fabricated at a 3:1 scale. Filled regions include FEA simulations within the range $\tau_i^* \leq \tau \leq n\tau$. (F) Experimental relaxation curve. Times τ_i^*, τ and nτ, respectively considered for the numerical analysis of viscosity effects. Experiments were performed at a test speed which correspond to a relaxation time τ_i^*=180 s.

S.2.5 Monomaterial Kresling cells: Complementary Results

The load paths and stored energy landscapes of the rubbery photopolymers DM60, DM70 and DM85 are shown in Fig. S.34. They exhibited monostability and complement the analyses presented for monomaterial Kresling cells, as described in section 2.5.

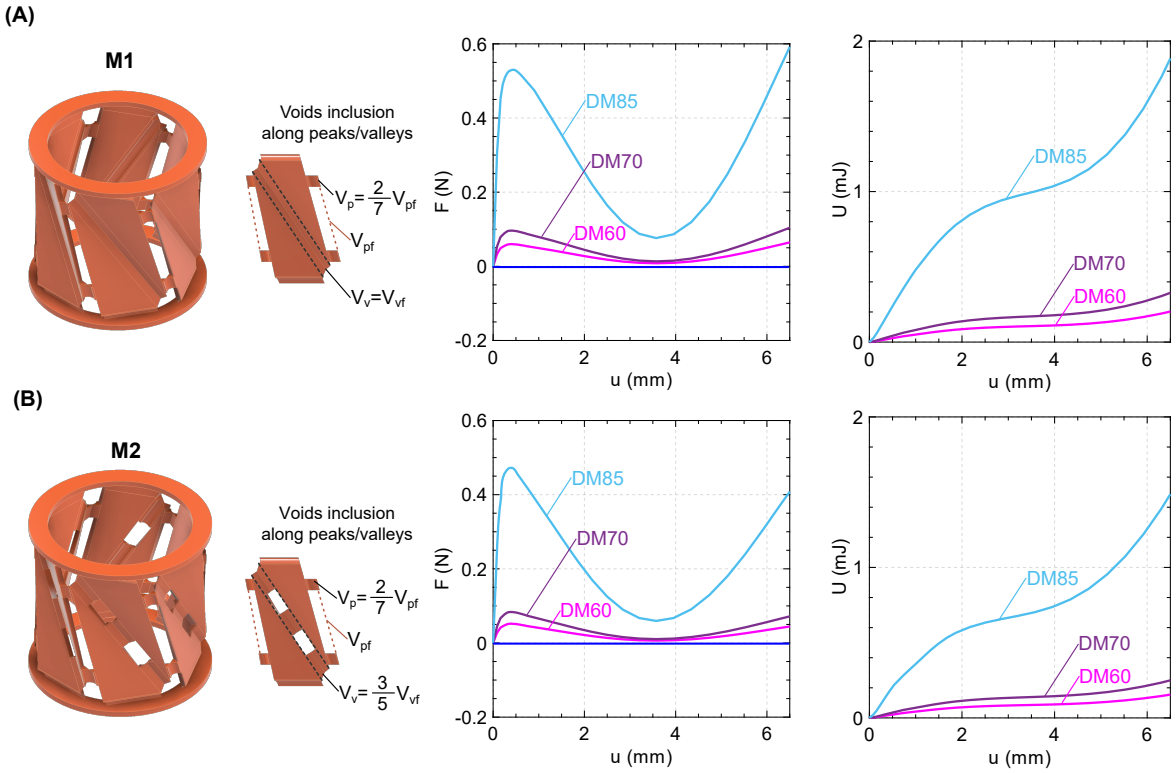

Figure S.34: Load paths and energy landscapes of Monomaterial Kresling cells. Cases with variable void inclusions along the creases: **(A)** M-1 and **(B)** M-2. Results of Kresling cells at a 1:1 scale.

S.3 Captions for Supplementary Videos

Caption for Video S1. Experimental validation of the parametric study on crease geometry of 3D printed Kresling cells. Comparison between Numerical (FEA) and Experimental (Exp) load path results from compressive tests on the C8 case. Kresling cell creases, generated with reduction factors RF = 0.80, 0.66, and 0.50, exhibited bistable or monostable behavior.

Caption for Video S2. Hands-on Experimental validation of Bistability in 3D printed Kresling cells. Evidence of bistable or monostable behavior in various Kresling cells with creases made of DM60. The creases were generated with reduction factors in the range of $0.25 \leq RF \leq 0.80$ and an intact crease case (INT).

Caption for Video S3. Experimental validation of the crease degradation in 3D printed Kresling cells. Effect of rubbery crease cross-section degradation on the load path, observed after three sequential experiments on the same sample (C8, RF=0.80, creases made of DM60).

Caption for Video S4. Effects of viscosity on bistable Kresling cells: Hands-on experimental validation. Evidence of bistable or monostable behavior in Kresling cells (C8, RF = 0.80) with creases made of rubbery materials that have different viscosity and relaxation modulus compared to DM60 (G_{60}=0.220 MPa):AG30 ($G_\infty=0.7G_{60}$), DM70 ($G_\infty=1.4G_{60}$), DM85 ($G_\infty=2.6G_{60}$), and DM95 ($G_\infty=3.9G_{60}$).

Caption for Video S5. Programmable Monostable Kresling Assemblies. Compression test, folding process, and load paths from numerical (FEA) and experimental (EXP) analysis for the following cases: (i) all creases made of DM60, (ii) stiffer creases (DM95) in the even layers, and (iii) stiffer creases (DM95) in the odd layers. Numerical simulations stopped at the first contact between panels.

Caption for Video S6. Prototyping of 3D printed Kresling cells via Polyjet technique. Different stages of fabrication and post-processing for multi-material 3D-printed Kresling cells using a Stratasys J750 printer within the PolyJet framework.

References

[1] Z. Zhai, Y. Wang, H. Jiang, Origami-inspired, on-demand deployable and collapsible mechanical metamaterials with tunable stiffness, Proceedings of the National Academy of Sciences 115 (9) (2018) 2032–2037.

[2] R. Masana, M. F. Daqaq, Equilibria and bifurcations of a foldable paper-based spring inspired by kresling-pattern origami, Physical Review E 100 (6) (2019) 063001.

[3] S. Zang, D. Misseroni, T. Zhao, G. H. Paulino, Kresling origami mechanics explained: Experiments and theory, Journal of the Mechanics and Physics of Solids (2024) 105630.

[4] H. Yasuda, T. Tachi, M. Lee, J. Yang, Origami-based tunable truss structures for non-volatile mechanical memory operation, Nature Communications 8 (1) (2017) 1–7.

[5] Dassault Systèmes, Abaqus Documentation, Hyperelastic behavior of rubberlike materials, version 6.10 (2010).

[6] F. F. Abayazid, M. Ghajari, Material characterisation of additively manufactured elastomers at different strain rates and build orientations, Additive Manufacturing 33 (2020) 101160.

[7] C. Tzikang, Determining a prony series for a viscoelastic material from time varying strain data, Tech. rep., NASA (2000).

[8] H. Cho, J. C. Weaver, E. Pößelt, P. J. in't Veld, M. C. Boyce, G. C. Rutledge, Engineering the mechanics of heterogeneous soft crystals, Advanced Functional Materials 26 (38) (2016) 6938–6949.

[9] S. Mora, N. M. Pugno, D. Misseroni, 3d printed architected lattice structures by material jetting, Materials Today (2022).

[10] D. Bigoni, Nonlinear solid mechanics: bifurcation theory and material instability, Cambridge University Press, 2012.